Application of a Scale Normalization Technique for High Resolution Analysis of the Magnetosheath at Mars

Jacob Fruchtman, Jasper Halekas, Francis Eparvier, Jacob Gruesbeck, Christian Xavier Mazelle, David Mitchell

JGR Space Physics

RESEARCH ARTICLE
10.1029/2024JA033166

Application of a Scale Normalization Technique for High Resolution Analysis of the Magnetosheath at Mars

Jacob Fruchtman[1], Jasper Halekas[1], Francis G. Eparvier[2], Jacob Gruesbeck[3], Christian Mazelle[4], and David Mitchell[5]

[1]1Department of Physics and Astronomy, University of Iowa, Iowa City, IA, USA, [2]University of Colorado, Boulder, CO, USA, [3]Solar System Exploration Division, NASA Goddard Space Flight Center, Greenbelt, MD, USA, [4]Institut de Recherche en Astrophysqiue et Planétologie, Université de Toulouse, CNRS, UPS, CNES, Toulouse, France, [5]Space Sciences Laboratory, University of California, Berkeley, CA, USA

Key Points:

- A new system-dependent spatial binning technique better resolves shock fine structure and magnetosheath forces than Cartesian bins
- At the bow shock, ion pressure diverges asymmetrically due to temperature anisotropy and magnetic pressure gradient scales with Mach number
- At the Martian magnetosheath, the mirror mode instability growth is sensitive to the solar zenith angle, affecting plasma thermalization

Supporting Information:

Supporting Information may be found in the online version of this article.

Correspondence to:

J. Fruchtman,
jfruchtman@uiowa.edu

Citation:

Fruchtman, J., Halekas, J., Eparvier, F. G., Gruesbeck, J., Mazelle, C., & Mitchell, D. (2024). Application of a scale normalization technique for high resolution analysis of the magnetosheath at mars. *Journal of Geophysical Research: Space Physics*, *129*, e2024JA033166. https://doi.org/10.1029/2024JA033166

Received 12 AUG 2024
Accepted 26 NOV 2024

Author Contributions:

Conceptualization: Jacob Fruchtman
Data curation: Jasper Halekas, Francis G. Eparvier, Jacob Gruesbeck, Christian Mazelle, David Mitchell
Formal analysis: Jacob Fruchtman, Jasper Halekas
Funding acquisition: Jasper Halekas
Investigation: Jacob Fruchtman
Methodology: Jacob Fruchtman, Jacob Gruesbeck
Project administration: Jasper Halekas
Resources: Jasper Halekas, Francis G. Eparvier, Jacob Gruesbeck, Christian Mazelle, David Mitchell

Abstract In order to study spatial distributions of global magnetosheath structures, physicists often rely upon spatial binning, whereby space is divided into cells, each filled with the average value of all spacecraft measurements within that cell. The traditional binning schema utilizes a fixed Cartesian grid of cube bins. The morphology of the magnetosheath's boundaries are not fixed, however, but driven by upstream and planetary conditions. Therefore, the spatial structures are not fixed in Cartesian space, and thus a Cartesian binning technique will produce a highly coarse grained spatial distribution. We propose an alternative binning technique utilizing a scale normalized dimensionless coordinate system defined in terms of magnetosheath morphology. To demonstrate the efficacy of this technique, we apply a basic implementation to the Martian system. We are thereby able to achieve a high-resolution spatial mapping of bow shock and magnetosheath processes and resolve spatial structures that are washed out when binned traditionally. In particular, we can resolve the shock overshoot, analyze the dominant forces acting at the shock, and obtain fine-scale distributions of the bulk ion plasma magnetosheath forces and thermalization mechanisms. Magnetic tension and magnetic pressure gradient are compared. The ion pressure divergence at the shock is found to significantly vary in line with the solar wind temperature anisotropy. The dependency of the mirror mode instability on location and Mach number, and its implications for thermalization processes in the small Martian magnetosheath are investigated.

Plain Language Summary We aim to study how solar wind plasma changes as it travels through the magnetosheath, focusing on the varying structures within the plasma at different locations. Specifically, we are interested in how conditions of the solar wind plasma before it reaches the magnetosheath outer boundary, the bow shock, influence the magnetosheath. Most processes that develop within the magnetosheath are directly dependent on the state transformation of the plasma at the bow shock and how long since the plasma transited the boundary. To analyze these structures, we create spatial maps by plotting spacecraft measurements. This involves dividing space into 3D cells and averaging measurements taken when the spacecraft is in each cell. Traditionally, cube-shaped cells of fixed size and position are used. However, because the bow shock's size and shape vary, structures may not align with these fixed cells, resulting in low-resolution images. In this paper, we introduce a new method of dividing space into cells that maintain consistent positions relative to the bow shock, regardless of its size or shape. Applying this method to the Martian magnetosheath, we achieve much higher resolution images than with the standard method. This allows us to observe previously obscured structures and reveal new findings.

1. Introduction

Outside of the solar corona and within the heliosphere, there are two important types of magnetized plasma regions. The first is the solar wind (SW), which blows out from the sun and ultimately makes up the heliosphere itself. The second are the plasmas contained within magnetospheres, cavities in the solar wind which (magnetically) separate the inner and outer plasmas. These occur where the SW's dynamic 'ram' pressure $P_d = \rho_{SW} V_{SW}^2$ is less than the inner magnetospheric pressures, thus requiring the SW and frozen-in Interplanetary magnetic field (IMF) to slow and be diverted around. Not all magnetospheres are generated from planetary magnetic fields. Venus, Mars, and comets have magnetospheres which are externally induced (Luhmann et al., 2004): In the dayside upper exosphere, ions are generated by photoionization by extreme ultraviolet radiation (EUV) and charge-exchange by the SW plasma, and (to a much lesser extent) by electron impact ionization (Kallio

Software: Jacob Fruchtman, Jasper Halekas
Supervision: Jasper Halekas
Validation: Jacob Fruchtman, Christian Mazelle
Visualization: Jacob Fruchtman
Writing – original draft: Jacob Fruchtman
Writing – review & editing: Jacob Fruchtman, Jasper Halekas, Christian Mazelle

et al., 1997; Mazelle et al., 2018; Rahmati et al., 2018). Within the volume where the thermal pressure P_{TH} of these planetary (or comet) ions (and electrons) exceeds the ram pressure, an ionosphere is created as an initial obstacle. For newborn ions outside of this volume, the motional electric field of the SW causes them to be 'picked up'. The successive generation of pick-up ions results in a macroscopic 'mass loading' effect that further slows down the SW by conservation of momentum. From outside, the ionosphere resembles a conducting sphere. The IMF -which is being dragged toward the ionosphere by the SW—slowly varies over time. These magnetic fields produce superficial currents in the ionosphere that generate opposing magnetic fields thereby preventing the IMF from penetrating the ionosphere. This results in the 'pile-up' of IMF lines around the ionosphere until the magnetic pressure $P_B = B^2/2\mu_0 > P_d$ and thus generating a 'Magnetic Barrier' or 'Magnetic Pileup Region' (MPR) which the solar wind cannot enter (e.g., Bertucci et al. (2005) and references therein after). The outer boundary of this MPR is called the Magnetic Pileup Boundary (MPB).

Within a plasma, information (about a perturbation of the medium) cannot propagate above a fast magnetosonic Mach number $M_{fms} = |\mathbf{v} \cdot \hat{\mathbf{n}}_{wave}|/V_{fms}$ corresponding to wavespeed

$$V_{fms}^2 = 0.5\left[\left(c_S^2 + v_A^2\right) + \sqrt{\left(c_S^2 + v_A^2\right)^2 - 4c_S^2 v_A^2 \cos^2\theta_{BN}}\right]$$

where c_S, and v_A are the sound and Alfven speeds and $\theta_{BN} = \cos^{-1}(\mathbf{B} \cdot \hat{\mathbf{n}}_{wave}/|\mathbf{B}|)$. With respect to the planetary obstacle, the incoming SW is super-fast magnetosonic. Thus when information about the MPB counter-propagates through the SW in the form of magnetosonic compression waves, they cannot travel infinitely, but instead build up at some distance to form a 'bow' shock (BS) surface (Kennel et al., 1985).

With certain exceptions outside the fluid description, these compression waves cannot propagate further upstream from the BS. Thus all deflection of the SW must start at the BS and continue downstream. The region between the BS and MPB where the solar wind has been shocked, slowed, heated, and compressed, and where deflection can occur, is called the magnetosheath. Under the MHD description, the magnetosheath is the shocked downstream region of a plasma and so largely obeys the MHD Rankine-Hugoniot equations (e.g., Russell et al. (2016)). In particular, the downstream plasma initially (theoretically) obeys the jump conditions n_D/n_U, $(V_i)_D/(V_i)_U$, $(B_i)_D/(B_i)_U$, and T_D/T_U determined entirely by upstream conditions. Note that, as observed in Fruchtman et al. (2023), this is not always observed to be true at Mars - mainly due to the small size of its magnetosheath. However, it is a good first starting point to consider the jump conditions valid to relate the upstream and downstream plasma states.

Ions gyrate along field lines. At the shock, field lines become compressed, and so the plasma is primarily thermally compressed perpendicular to the magnetic field. In addition, ion reflection at the supercritical shock also pumps energy into the perpendicular direction. Thus, the ion temperature anisotropy $A_i = T_{i\perp}/T_{i||}$ should suddenly increase at the shock. As a result, a magnetosheath is characterized by increased temperature anisotropy, enabling the presence of mirror mode structures (e.g., Jin et al. (2022)).

1.1. Martian Bow Shock Drivers

In this paper, we concern ourselves with the Martian magnetosheath. As the outer surface is set by the BS, it is necessary to understand how the BS varies in order to characterize the magnetosheath. This variation in turn mostly varies due to the BS's external drivers.

It has been found that the BS contracts with increasing P_d and flow directed magnetosonic mach number $M_{ms} = |\mathbf{V}_{SW}|/\sqrt{c_S^2 + v_A^2} \geq M_{fms}$ (Hall et al., 2016; Halekas, Ruhunusiri, et al., 2017; Gruesbeck et al., 2018; Garnier et al., 2022a; N. J. T. Edberg et al., 2010). It should be noted that M_{ms} is itself slightly anti-correlated with solar intensity in the context of the 11 years solar cycle (Fruchtman et al., 2023).

Martian orbit has an eccentricity of $\varepsilon_M = 0.0935$ (Williams, 2021). Thus, given the r^{-2} drop off in radiation, the solar EUV irradiance has an orbital variation of ±20%. This is in addition to irradiance in the Lyman α band varying by almost a factor of two over the course of the 11 years solar cycle (Hall et al., 2019; Kotzé, 2023). Increased EUV should correspond to both a puffed up exosphere and increased mass loading (Hall et al., 2016). It

has been found that the BS expands with increased EUV irradiance (N. Edberg et al., 2008; Hall et al., 2016; Halekas, Ruhunusiri, et al., 2017; Gruesbeck et al., 2018; Garnier et al., 2022a, 2022b).

Given the contribution to BS formation provided by IMF draping, the orientation of the IMF should also contribute. Statistical analysis by Vignes et al. (2002) and simulations by M. Wang et al. (2020) showed possible dependence of the BS on cone angle $\theta_{VB} = \arccos\left(\frac{\mathbf{V}_{SW}\cdot\mathbf{B}_{IMF}}{|\mathbf{V}_{SW}||\mathbf{B}_{IMF}|}\right)$ and clock angle $\arctan(B_{IMF_Y}/B_{IMF_Z})$, but was later shown to be insignificant by Garnier et al. (2022a). Vignes et al. (2002) suggested a possible asymmetry along the direction of the motional electric field $\mathbf{E} = -\mathbf{V}_{SW} \times \mathbf{B}_{IMF}$, though later analyses have ruled this out as vestigial crustal field influences (Gruesbeck et al., 2018).

The direction of the IMF does have local effects on morphology: The plasma and magnetic compressions of the magnetosheath increase with the shock normal angle θ_{BN} between the BS surface normal $\hat{n}_{BS}$ and upstream **B** (IMF) direction (Kennel et al., 1985). Morphology wise, this is accompanied by a significant decrease in BS standoff distance at low 'quasiparallel' θ_{BN} (Garnier et al., 2022a; Ma et al., 2004; Vignes et al., 2000; Zhang et al., 1991). Given that the IMF is directed along the Parker spiral rather than parallel with the Mars-sun-line such that the dawn and dusk sides of the planet experience different average θ_{BN}, this manifests as a "dawn-dusk" asymmetry (Gruesbeck et al., 2018; Ma et al., 2004).

At Mars, there additionally exist remanent sources of 'crustal' magnetic fields which are more prominent in the southern hemisphere (Acuña et al., 1998; Connerney et al., 2015). These act to substantially push upward the local MPB and -to a lesser extent-the local BS (Crider, 2004; Fang et al., 2017; Garnier et al., 2022b; Němec et al., 2020). This expansion occurs globally to some extent when the strongest crustal field regions are on the day side of the planet (Garnier et al., 2022b; Gruesbeck et al., 2018).

There has been observed a prominent asymmetry between ecliptic hemispheres within aggregated data (Mazelle et al., 2004), including MAVEN data (Gruesbeck et al., 2018). While initially believed to be the result of a crustal field asymmetry - Mars only has a 25° axial tilt (Williams, 2021) - Garnier et al. (2022b) showed this to more likely be systematic biasing due to the evolving MAVEN spacecraft orbital geometry across a solar cycle. Instead, the crustal fields more predominantly induce a global perturbation dependent on the angular distance from the crustal field sources to the subsolar point.

Using cross-correlation techniques, Garnier et al. (2022a) showed that EUV and M_{ms} are the most significant independent drivers of variation in the BS morphology, with θ_{BN} and the crustal fields holding significant second order importance.

1.2. Frameworks for Studying Spatially Varying Structures

A reliable approach to analyzing plasma structures and processes involves analyzing the spatial variation in the plasma. For space plasmas where it is not possible to measure everywhere at once, it is necessary to do so statistically by building spatial distributions of spacecraft data. To measure the variation in some quantity, one can divide space into a three dimensional array of cells, with corresponding cells for the chosen quantity, and take the average value of that quantity as measured by the spacecraft whenever it is present in that cell. The conventional way of constructing this grid is by using a fixed Cartesian coordinate system. Examples of this can be observed in Halekas, Brain, et al. (2017); Rahmati et al. (2018); Simon Wedlund et al. (2023). This is accurate if the system one is concerned with is fixed in size. As we illustrate in Figure 1a, the conventional method is problematic for magnetosheaths. The planet's bow shock acts as a boundary surface that sets the initial conditions for the magnetosheath plasma. The bow shock location *is not* fixed: Its size and shape are sensitive to upstream conditions. Thus the locations of magnetosheath subprocesses -which are also controlled by these upstream parameters-are not fixed either. This means that when applying a Cartesian binning scheme, a given bin will average over multiple processes at different times and conditions, and conversely, any given -potentially infinitesimal-subprocess will be smeared over multiple bins. Fine scale structure is lost.

A more accurate binning schema would be one dependent on the morphology of the system, and for which the primary coordinate is chosen such that the "origin" along that axis is the initial bow shock boundary surface. In addition, the distance scale from the shock used for defining bin sizes should not be in raw SI units of length, but some dimensionless quantity such that lengths have been normalized to scales appropriate to the system. Furthermore, given that the magnetosheath is compressible and has an inner boundary which the downstream

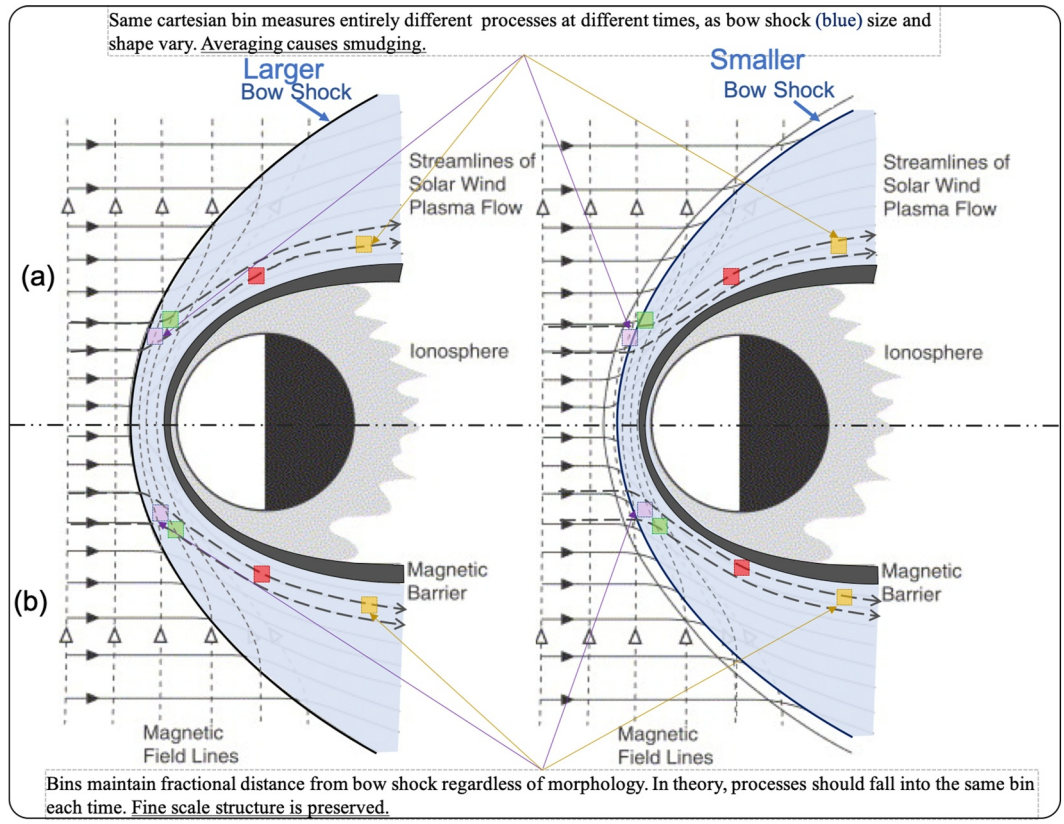

Figure 1. Diagram of binning methods applied to induced magnetosphere system. The bow shock is drawn as the dark blue curve, and magnetosheath as the light blue region. Left and right diagrams show larger and smaller bow shock boundaries respectively. Thick and thin dashed lines show plasma streamlines and magnetic field lines respectively, scaled with bow shock and maintaining footpoints. Each colored square represents the location of a bin, fixed to the chosen coordinate system. (a) Cartesian binning schema: Regardless of bow shock size, bins stay fixed in Cartesian space. (b) Scale normalized fractional distance binning schema: Bins move to maintain fractional distance from the bow shock. Source of original diagram (Russell et al., 2006).

solar wind plasma asymptotically approaches but never crosses, we can approach this as a double sided boundary value problem: a reasonable ansatz is that the fluid can be considered to hold a state 'A' at outer surface A, a state 'B' at inner surface B, and the states in between will be constrained to experience the sequence of internal sub-processes allowing for a spatial transition from state 'A' to 'B'. These subprocesses should be present regardless of the distance between boundaries - the distances between them only expanding and compressing as the system expands or compresses - and thus be considered to be 'fixed' in the interior of the system to certain *fractions* of the distance between the boundaries. We can therefore consider a different coordinate schema which should allow fine structure to be preserved, as illustrated in Figure 1b: a normalized dimensionless coordinate system wherein the primary "radial" coordinate D_{frac} is some form of fractional distance from the shock. Since the locations of sheath processes should scale with the bow shock morphology for a given set of upstream parameters, this should reliably capture each process in its own bin.

Here, we introduce a new framework for studying the morphologically dynamic induced magnetosheath at higher precision. We then use it in order to study at higher resolution how the magnetosheath varies with these upstream conditions, and analyze the scientific results which arise from applying this framework to the Martian magnetosheath.

2. MAVEN

The MAVEN spacecraft has been orbiting Mars since September 2014, and collecting data since November 2014 (Jakosky et al., 2015). It has a large suite of instruments for analyzing the local environment. In our study we utilize the data from four of these instruments:

The MAG instrument measures local magnetic field data at 32 Hz resolution (Connerney et al., 2015). It has two versions of L2 data corresponding to 1 and 0.25 s time-series bins respectively. For file size reasons, we use the 1 s data.

The primary solar wind ion analyzer for MAVEN is the Solar Wind Ion Analyzer (SWIA) (Halekas et al., 2015). SWIA has fine survey (SWIFS) and coarse survey (SWICS) modes, intended for undisturbed solar wind, and sub-bow shock plasma measurements respectively. These have two different spatial resolutions and fields of view. SWIFS measures ion data from an inner $45^\circ \times 45^\circ$ sunward pointing FOV region with smaller - $3.5^\circ \times 4.5^\circ$ angular resolution - bins. The rest of the SWIA detector's 90°x360° FOV uses larger - $22.5^\circ \times 22.5^\circ$ angular resolution - bins. SWICS data utilizes the full field of view, combining multiple SWIFS bins together for consistent bin size. For consistency, we use SWIFS to calculate characteristic upstream time-averaged ion moments, and SWICS for instantaneous time-series measurement data. In the undisturbed solar wind, there are two peaks in the energy distribution corresponding to H^+ and He^{++} species, from which can be calculated separate temperature moments T_{proton} and T_{alpha} (Halekas, Ruhunusiri, et al., 2017). For the purposes of calculating upstream M_{ms}, we use T_{proton} rather than T_{SWIFS}.

Alongside an instrument for ion data, there is also a MAVEN solar wind electron analyzer called the Solar Wind Electron Analyzer - or SWEA (Mitchell et al., 2016). To obtain SWEA moments, we utilize the 4 s cadence SPEC mode data after correcting for the spacecraft potential. Between the time of data aggregation and this writing, SWEA's algorithm for calculating electron moments was updated to - among other issues - account for a low-energy anomaly which offset moments by an order of magnitude starting 2019-11-16. As such we did not aggregate any data after 2019-11-15.

The Extreme Ultraviolet Monitor (EUVM) is the solar extreme ultraviolet monitor for MAVEN (Eparvier et al., 2015). EUVM's L2 EUV irradiance data is measured in three wavelength channels, and provides a quality flag. The third channel provides Lyman alpha Irradience (Lyα). There are orbits where the spacecraft attitude or other operational constraints are not optimal to make EUVM measurements, and therefore we use a daily average of good quality Lyman Alpha irradiance rather than instantaneous measurements.

For purposes of consistency and ease of calculating derived quantities, we interpolate our plasma moment data to 1 s resolution, and use daily average EUVM data.

3. Methodology

To begin, it should be noted that local upstream conditions $\{A\}$ should control not just the magnetosheath morphology, but also the internal structures and processes. We split Martian magnetosheath data into cadres based on whether their corresponding upstream conditions are above or below the sample median. Thus if the distribution of half-orbits is partitioned based on N different average local upstream conditions, there will be 2^N cadres. We can then apply our framework to each cadre.

3.1. Dimensionless Pseudo-Spherical Coordinate System

The primary coordinate system for dealing with the Martian plasma system is the Mars-centered Solar Orbital (MSO) coordinate system, where $\hat{x}_{MSO}$ points from the core toward the Sun, $-\hat{y}_{MSO}$ points in the direction of Martian orbital velocity, and $\hat{z}_{MSO}$ completes the triad. The second coordinate system used to study Martian plasma is the Mars-Solar-Electrical (MSE) coordinate system. In this system, $\hat{x}_{MSE}$ is antiparallel to the SW velocity, $\hat{z}_{MSE}$ is parallel to the SW motional electric field $\mathbf{E} = -\mathbf{v}_{SW} \times \mathbf{B}_{IMF}$ and $\hat{y}_{MSE}$ completes the system. We would like to be able to convert time-series data from these coordinate systems to a pseudo-spherical coordinate system referenced to the BS position.

To implement our framework, we make a series of motivated simplifications and assumptions.

First we note that the inner surface of an induced magnetosheath is the MPB. Rigorously, a morphologically dependent and scale normalized coordinate system should have as one coordinate the fractional distance from the outer boundary surface to a corresponding point on the inner surface. At Mars, not only is this inner surface azimuthally asymmetric, but its surface is also locally highly perturbed by the presence of crustal fields below (Crider, 2004; Fang et al., 2017). As of the time of this study, there does not exist a 3D parameterization of the MPB surface which includes the drivers of the MPB's morphology. As such, we make the simplification of defining our "radial" coordinate as the fraction of the *radial* distance from the shock to the surface of the planet:

$$D_{frac} = \frac{r - R_{BS}}{R_{BS} - R_M} \tag{1}$$

So defined, $D_{frac} = 0$ at the radius of the shock discontinuity (to best possible accuracy) and $D_{frac} = -1$ at average Mars surface radius $R_M = 3389.5$km. Note that because the MPB does not maintain a fixed fractional radial distance between our chosen surfaces, accuracy in binning plasma processes together will decrease with fractional distance from the BS based on the same principles discussed above for issues in Cartesian binning. This implementation will therefore work best close to the BS (which is mostly where we're interested). Processes close to the MPB may be binned on the other side of the boundary. However, as the size of the MPB both does not change significantly compared to the BS and is subject to the same drivers as the BS (Ramstad et al., 2017), the inaccuracies arising from choice of inner boundary should not be significant.

For our next simplification, to calculate R_{BS} we assume that the BS surface in each cadre j obeys a simplistic perturbation theory model for embedded surface coordinates $\{\Omega\}$ and drivers $\{A\}$:

$$\begin{aligned} R_{BS}(\{\Omega\},\{A\}) &= R_{BS}\left(\{\Omega\},\left\{A_j^{(0)}\right\} + \{\delta A\}\right) \\ &= (1 + \epsilon(\{\Omega\},\{\delta A\}))\, R_{BS}^{(0)}\left(\{\Omega\},\left\{A_j^{(0)}\right\}\right) \end{aligned} \tag{2}$$

Here, $R_{BS}^{(0)}\left(\{\Omega\},\left\{A_j^{(0)}\right\}\right)$ is some average surface and $|\epsilon(\{\Omega\},\{\delta A\})| \ll 1$ is to be chosen such that the model intersects locations where the MAVEN spacecraft is identified as crossing the BS.

Following the results of Marquette et al. (2018); Azari et al. (2023) we assume for simplicity (and given the restrictions to single point measurements) that in each half-orbit k of the spacecraft corresponding to a bow shock crossing, a small enough period of time has passed such that the morphology and upstream conditions are static and in agreement with local measurements. That is, a single (time-averaged) measurement of the local upstream solar wind conditions can be taken as specifying "the" upstream conditions $\left\{A_k = A_j^{(0)} + \delta A_k\right\}$ during the entire sub-orbit interval when the spacecraft is downstream of the shock, and that a single parameterization of the bow shock surface $R_{BS}(\{\Omega\},\{A_k\}) = R_{BS,\,k}(\{\Omega\})$ -which intersects the measured bow shock crossing position - will be accurate for each entire half-orbit interval. By extension, this means we need only a single $\epsilon(\{\Omega\},\{\delta A_k\}) = \epsilon_k(\{\Omega\})$ per half-orbit.

The form of our parameterization $R_{BS,\,k}$ is itself constrained by implementation concerns. First, consistency within each cadre requires the form of $R_{BS,\,k}(\{\Omega\})$ to be preserved - if with different coefficients for each half orbit. Second, the spatial variation is more intuitive to analyze in figures with Cartesian axes. As plotting the binned quantities in our new coordinate system would require a difficult method to implement irregular grid of data, we would instead like to return to Cartesian coordinates after normalizing our scale, for plotting purposes. Third, an analytic form of the Jacobian is required if we are to engage in any form of vector calculus. However, limited information about each half-orbit can be preserved when binning is performed given finite dataset size. Thus in each cadre, vector calculus and return to Cartesian requires the use of a single overall surface $R_{BS}^{(0)}$ of the same form as $R_{BS,\,k}$.

Unavoidably, this means that ϵ cannot contain the perturbation in BS due to the day-night rotation of the strong crustal field region, and must instead take the form of a single argument ϵ_k. That is, the bow shock is assumed to maintain its shape and just expands/contracts from the average surface. To make calculations simpler, we use the spherical angular coordinates $\Omega = \{\theta = \arccos(x/r),\ \phi = \arctan(y/z)\}$ as our second and third coordinates

rather than more rigorously deriving embedded coordinates in the shock surface which are roughly parallel to the surface. It should be noted that the direction of the solar wind velocity $-\hat{x}_{MSE}$ deviates from antisunward by approximately 4°. As this is a small angle, we will make the simplifying approximation $\hat{x}_{MSE} = -\hat{v}_{sw} = \hat{x}_{MSO}$, so that we can use the Solar Zenith Angle (SZA) as the polar angle for both the MSO and MSE coordinate frames. This means that our chosen coordinate system uses dimensionless coordinates:

$$\{D_{frac}, \mathrm{SZA}, \phi\} \tag{3}$$

Gruesbeck et al. (2018) modeled the BS as 3D quadric surfaces in Cartesian MSO and MSE frames by fitting almost 2000 shock crossing locations to the general quadric equation

$$c_0 x^2 + c_1 y^2 + c_2 z^2 + c_3 xy + c_4 yz + c_5 xz + c_6 x + c_7 y + c_8 z = 1 \tag{4}$$

and modeled more precise surfaces by choosing subsets of the data corresponding to different upstream conditions greater or less than some median value. Fruchtman et al. (2023) automatically and precisely identified the center of 3845 BS crossings between 2014 and 2019, and measured average values of local upstream raw quantities (henceforth denoted $\langle A \rangle_U$ for the characteristic upstream time average of raw quantities A) -from which we can calculate derived quantities - which can be found in Fruchtman (2023). This latter dataset contains almost twice the number used for Gruesbeck et al. (2018), we add an increased level of precision by calculating average surface coefficients $\{c\}$ for cadres based on $N = 2$ choices of upstream condition for more precise models. Converting to spherical coordinates allows for a parametrization $R_{BS}^{(0)}(SZA, \phi, \{c\})$. We calculate quadric surfaces for both the MSO and MSE frame.

We thus assume that the surface in each half-orbit is only slightly perturbed in scale (but not shape) from the average surface so that, all together, Equation 2 becomes

$$\begin{aligned} R_{BS,\,k}(SZA, \phi) &= (1 + \varepsilon_k) R_{BS}^{(0)}(SZA, \phi, \{c\}) \\ &= \left(\frac{r_k}{R_{BS}^{(0)}\left(SZA_k, \phi_k, \{c\}\right)} \right) R_{BS}^{(0)}(SZA, \phi, \{c\}) \end{aligned} \tag{5}$$

where, r_k, SZA_k and ϕ_k are the spherical coordinates of the k^{th} measured MAVEN shock crossing location. We can then fully define the dimensionless, scale-normalized, fractional distance D_{frac} as

$$D_{frac} = \frac{r - R_{BS,\,k}(SZA, \phi)}{R_{BS,\,k}(SZA, \phi) - R_M} \tag{6}$$

For the purposes of vector calculus (Eisele & Mason, 1970, Chapter three) and returning to Cartesian coordinates for plotting of spatial distributions, we use our small perturbation ansatz and make the zeroth order approximation for a radius r:

$$r = \left(R_{BS}^{(0)}(SZA, \phi, \{c\}) - R_M\right) D_{frac} + R_{BS}^{(0)}(SZA, \phi, \{c\}) \tag{7}$$

Here, D_{frac}, SZA, and ϕ are the coordinates for any arbitrary position within the system, so that $R_{BS}^{(0)}(SZA, \phi, \{c\})$ outputs the radius of the cadre's average BS surface at those angular coordinates.

A subset of the BS asymmetries - those that depend on local time (the dawn-dusk asymmetry) and geographic position (the southern crustal field asymmetry) - are lost when calculating the average surface in MSE coordinates. Comparatively, the asymmetries that arise in the MSE frame are much smaller in scale (as can be seen from the relative rotational symmetry in the tabulated coefficients within Gruesbeck et al. (2018)). The true fractional distance from the bow shock to the planet shouldn't change regardless of the choice of (Mars centered) reference frame. As such, we always utilize D_{frac} as calculated in MSO coordinates from the MSO coordinate surfaces regardless of whether or not we rotate our data into the MSE frame. It should be noted that this means that once the data has been rotated into MSE and binned in pseudospherical coordinates, any steps requiring

consideration of the BS morphology (e.g., returning to Cartesian coordinates or vector calculus) will involve a mix of MSO derived D_{frac} and MSE derived $\{c\}$. We include our best fit coefficients $\{c\}$ for each cadre and coordinate frame in the attached text file "coeffs.txt", and supply further information in the supporting document.

3.2. Binning Schema

Our framework uses a multiple step process. As a preliminary step, we must first take into account which coordinate frame - MSO or MSE - we wish to use. If we wish to rotate into MSE coordinate system, we use the simplifying assumption $\hat{x}_{MSE} = \hat{x}_{MSO}$. Thus vectors and tensors can be rotated from MSO to MSE using the rotation matrix

$$\begin{bmatrix} 1 & 0 & 0 \\ 0 & \cos(\lambda) & \sin(\lambda) \\ 0 & -\sin(\lambda) & \cos(\lambda) \end{bmatrix}$$

where $\lambda = \arctan\left(\langle \mathbf{B} \rangle_U \cdot \hat{y}_{MSO} / \langle \mathbf{B} \rangle_U \cdot \hat{z}_{MSO}\right)$ is the clock angle of the local upstream IMF. Only then can binning take place. The subsequent binning schema is as follows.

1. First we bin quantities in our pseudo-spherical system. If we stay in the MSO frame, then we use as our third coordinate $\phi := \phi_{MSO} = \arctan\left(y_{MSO}/z_{MSO}\right)$, otherwise we use $\phi := \phi_{MSE} = \arctan\left(y_{MSE}/z_{MSE}\right)$. To enable high resolution figures, we choose for our bin sizes a resolution of $\Delta D_{frac} = 0.02$, and either 1deg or 2deg angular resolutions depending on whether our quantity is a scalar or not, respectively. For vectors and tensors, components are kept in Cartesian coordinates, for reasons discussed later. To focus on the sheath and near upstream region and maintain a reasonable array size, we consider only data within the fractional distance range $-1 \le D_{frac} < 1$.
2. In certain instances, we wish to perform operations (numerical derivatives, flow line tracing) on our grid space which require it to be mostly filled with data. In those cases, we NAN-fill our pseudo-spherical grid by creating a duplicate multidimensional array which is smoothed over to fill in the empty (NAN valued) cells. The NAN valued cells of the original array are then replaced with the interpolated cells.
3. We return to Cartesian for plotting spatial distributions by re-binning: We iterate through each pseudospherical cell, and bin the quantity in the cell corresponding to the position of the center of the cell in Cartesian space. It should be noted that azimuthal asymmetry in $R_{BS}^{(0)}(SZA, \phi, \{c\})$ will unavoidably lead to a spread in data (and thus coarse-graining) when projecting the spatial distribution into the cylindrical ($\rho = \sqrt{Y^2 + Z^2}$ vs. X) plane. To minimize this, all cylindrical projection figures in this document will utilize spatial distributions rotated into the more azimuthally symmetric MSE frame via the methods discussed above. For compactness, we will show the lengthscales in units of Megameters (Mm) rather than kilometers (km).

3.3. Numerical Vector Calculus Beyond Cartesian Position Space

Our framework can be applied not just to analyzing the spatial distribution of measured quantities, but also to forces calculated via vector calculus. For a finite resolution distribution of data, using numerical vector calculus on a field in a Cartesian grid space will produce coarse grained results anywhere where the field rapidly spatially varies in non-Cartesian directions. By much the same arguments as we have used for binning based on the morphology of the system, numerical vector calculus in a shock-based coordinate system should also improve our resolution.

In a non-Cartesian vector space, the components of either the covariant or contravariant form of a vector - and the covariant and contravariant derivatives with respect to these components - depend on position. It is thus overly complicated and susceptible to loss of precision to rotate the components of our vectors and tensors into this frame, apply relevant ∇ in that frame, and then rotate back into Cartesian frame. It is both simpler and still mathematically valid to keep the components in Cartesian form the entire way through, and use the chain rule to apply ∇ while in pseudospherical position space: For position vectors $q^s = \{D_{frac}, SZA, \phi\}$ and $x^i = \{x, y, z\}$ and arbitrary tensor $\mathsf{T}^{k_0 k_1 \cdots}(\mathbf{q})$ with Cartesian components, one need only calculate (using Einstein summation notation)

$$\nabla_i \mathrm{T}^{k_0 k_1 \cdots}(\mathbf{q}) = \frac{\partial \mathrm{T}^{k_0 k_1 \cdots}(\mathbf{q})}{\partial x^i} = \frac{\partial q^s}{\partial x^i} \frac{\partial \mathrm{T}^{k_0 k_1 \cdots}(\mathbf{q})}{\partial q^s} \tag{8}$$

where $\frac{\partial \mathrm{T}^{k_0 k_1 \cdots}(\mathbf{q})}{\partial q^s}$ can be calculated numerically in the pseudo-spherical coordinate system - taking into account periodic boundary conditions - for each Cartesian component k_ℓ separately, and $\frac{\partial q^s}{\partial x^i}$ are derived from the reciprocal basis vectors $\mathbf{a}^s = \frac{\partial q^s}{\partial x^i}\hat{\mathbf{e}}^i$ and then calculated analytically. To ensure orthogonality, the latter partial derivative is not differentiated directly. Were we to do so, the reciprocal basis vectors $\frac{\partial SZA}{\partial x^i}$ and $\frac{\partial \phi}{\partial x^i}$ would be entirely independent of morphology. Instead, we derive the basis vectors

$$\mathbf{a}_s = \frac{\partial x^i(\mathbf{q}, \{c_j\})}{\partial q^s}\hat{\mathbf{e}}_i \tag{9}$$

from which can be derived the reciprocal basis vectors (for each set of coefficients associated with a given cadre) via (Eisele & Mason, 1970, Chapter three)

$$\varepsilon_{ijk}\mathbf{a}^i = (\mathbf{a}_j \times \mathbf{a}_k)/(\mathbf{a}_1 \cdot (\mathbf{a}_2 \times \mathbf{a}_3)) \tag{10}$$

4. Data

The dataset we use for this study is comprised primarily of the time series within the half orbits corresponding to the 3,848 (relatively stationary) shock crossing locations listed in Fruchtman (2023) - along with the characteristic upstream parameters included therein, along with another 422 data points within our time range identified manually. Our 5 year period from 2015 to 11-15 to 2019-11-15 comprises almost the entire second half of Solar Cycle 24. For the purpose of focusing on the solar wind plasma, we constrain the intervals for these half-orbits such that their inner edge ends when one of three scenarios occur.

1. $SZA \geq 150$deg: Due to MAVEN's orbit geometry, almost all data at larger angles will be below the MPB, and is thus outside the scope of this study.
2. The MAVEN spacecraft passes behind the planet: That is, $X < 0$ and $\rho = \sqrt{Y^2 + Z^2} < R_M$.
3. The region identification algorithm (REGID) introduced in Halekas, Ruhunusiri, et al. (2017) determines that the spacecraft is within the ionosphere.

As the most significant independent global upstream drivers of BS morphology (Garnier et al., 2022a), we divided this data into cadres of derived upstream magnetosonic mach number $M_{ms} = |\langle \mathbf{V}^{ion} \rangle_U| / \sqrt{C_S^2 + V_A^2} \gtrless 6.73$, and $\mathrm{Ly}\alpha \gtrless 2.88 \mathrm{nW/m^2}$ based on the sample median values of upstream measurements associated with each shock. For calculation of C_S, we have used ion and electron adiabatic indices $\gamma_i = 5/3$ and $\gamma_e = 1$ respectively. It should be noted that there is not a homogeneous distribution of data points in $M_{ms} - \mathrm{Ly}\alpha$ space, and thus the sample medians may be far from the population medians. First, the parameters are relatively anti-correlated ($r = -0.241$) given their connection to solar activity. Second, the sub-orbits are not uniformly distributed in time: During the first several months of the mission (at highest Lyα) the ground based algorithm for computing spacecraft potentials would occasionally fail for the entire interval wherein MAVEN was upstream of the BS, thus preventing calculation of electron moments or M_{ms}.

The simplest global quantity to measure is the magnetic compression $B/\langle B \rangle_U$ across the shock. We will use it as proof of concept. The 1 day magnetic field profiles across the BS are well known. Upstream of the shock, the magnetic field is relatively quiescent. In quasiparallel shocks, this behavior is suddenly broken by a pulse train of increased $|\mathbf{B}|$ regions which slowly become thicker and closer together until merging entirely (Schwartz, 1991; Schwartz & Burgess, 1991). In the quasiperpendicular case (a majority of our collected half-orbits), the profile (in upstream and downstream solar wind) is characterized by the classic foot-shock ramp-overshoot-coherent downstream structure (Gedalin, 1996; Wong, 1968; Woods, 1971). The overshoot is a shock structure with thickness of the order of the upstream solar wind ion Larmor radius (Burne et al., 2021; Mellott & Livesey, 1987; Tatrallyay et al., 1997) continuing from the downstream side of the ramp, and its amplitude $B_{\max}/B_{down} - 1$ is significantly correlated with M_{ms} (Fruchtman et al., 2023).

In Figure 2 we show the spatial distribution of $B/\langle B\rangle_U$ in each cadre as rotated into cylindrical coordinates. We show for comparison the cylindrical average conic surface models of the BS and MPB as calculated in Trotignon et al. (2006). The top four panels show the result of the traditional binning method, while the bottom four show the result of our pseudo-spherical binning schema. When binning data into their real positions in space, structures like the BS are clearly fuzzy and smeared out. In the high M_{ms} cadres, an overshoot structure is barely visible, and does not appear at all in the lower cadres. Our scale normalization technique however, sharpens the shock surface into focus. A clear discontinuity is seen in all cadres. This makes more apparent that the BS jump is seen further from the Trotignon et al. (2006) fit for higher M_{ms} and lower Lyα. In addition, the Larmor radius thick shock overshoot is now coherent in all cadres, and its amplitude clearly increases with M_{ms} as previously observed. Also observed in Fruchtman et al. (2023) is the global trend whereby the magnetic compression decreases with SZA. While visible in standard binning cases, the trend becomes significantly sharper when our technique is applied.

5. Results

Having demonstrated the efficacy of our scale normalization schema, we now apply it to study the forces governing the bulk movement of the magnetosheath plasma, as well as the thermalization process within the plasma.

5.1. Forces

Using our pseudo-spherical coordinate system, we compute both the single ion species thermal pressure divergence $-\nabla\cdot \mathrm{P_{TH}}$ and $\mathbf{J}\times\mathbf{B} = (\nabla\times\mathbf{B})\times\mathbf{B}/\mu_0 = \mathbf{B}\cdot\nabla\mathbf{B}/\mu_0 - \nabla\left(\frac{B^2}{2\mu_0}\right)$. As we found that these forces do not significantly vary with Lyα, in this section we show the results for the high Lyα cadres only. For completeness and purpose of comparison, we include counterpart figures for the other cadres in our supporting document.

We show the spatial mapping of $(-\nabla\cdot \mathrm{P_{TH}})_{XMSE}$ in Figure 3 (top). As expected, we see a large outward pointing force at the shock surface corresponding to the sudden compression of the shocked plasma. In terms of spatial variation of the shock force, $(-\nabla\cdot \mathrm{P_{TH}})_{XMSE}$ is strongest (as expected) around the subsolar point. We also see the expected inward pointing force at the MPB, where the density of magnetosheath plasma of solar wind origin rapidly drops. Throughout the sheath, $-\nabla\cdot \mathrm{P_{TH}}$ otherwise acts to accelerate the plasma forward and laterally (not shown) after slowing it down at the shock. Comparing cadres, we also see M_{ms} dependent spatial variation at the BS: An azimuthal asymmetry in $(-\nabla\cdot \mathrm{P_{TH}})_{XMSE}$ can be observed, and is more significant for low M_{ms}. At high M_{ms}, there is a north-south asymmetry, with a stronger force in the ZMSE > 0 hemisphere. We note the presence of vertical stripes in the sheath where the sign flips. This is an artifact of a form of systemic error which will be discussed later.

Figure 3 (bottom) shows projections of $(\mathbf{J}\times\mathbf{B})_{XMSE}$ in the XY and XZ plane. It can be seen from the smaller color scale that the $\mathbf{J}\times\mathbf{B}$ force is weaker in the shock and sheath than $-\nabla\cdot \mathrm{P_{TH}}$. As expected, the $\mathbf{J}\times\mathbf{B}$ force points outward at the shock and MPB where the magnetic field amplifies the most. Also as expected, we once again see that $(\mathbf{J}\times\mathbf{B})_{XMSE}$ is strongest near the subsolar point. At the shock, we see that $(\mathbf{J}\times\mathbf{B})_{XMSE}$ decreases with M_{ms}. Also, in the X-Y plane, a more subtle asymmetry (compared to the thermal pressure gradient) is seen for lower M_{ms}, and in the X-Z plane, the force weakens at a higher rate toward the flanks for higher M_{ms}. This decrease with M_{ms} should arise from a similar trend in upstream M_A, which can be explained by splitting $\mathbf{J}\times\mathbf{B}$ into its constituent force terms.

We have calculated $\mathbf{J}\times\mathbf{B}$ as the difference between the magnetic tension and magnetic pressure gradient. As no study has yet analyzed these forces individually at Mars, we take advantage of the opportunity to do so here. The spatial variations are shown in Figure 4.

We see that $|\mathbf{B}\cdot\nabla\mathbf{B}/\mu_0|$ decreases rapidly with D_{frac}. The magnetic tension is a measure of the curvature of the magnetic field lines. The primary source of curvature within the sheath is the magnetic draping over the ionosphere. At distances further away from the ionosphere, simple geometry tells us that the curvature of field lines per unit volume will necessarily decrease. Though the trend is more obvious for the magnetic pressure gradient, the magnetic tension is also weaker for higher M_{ms}.

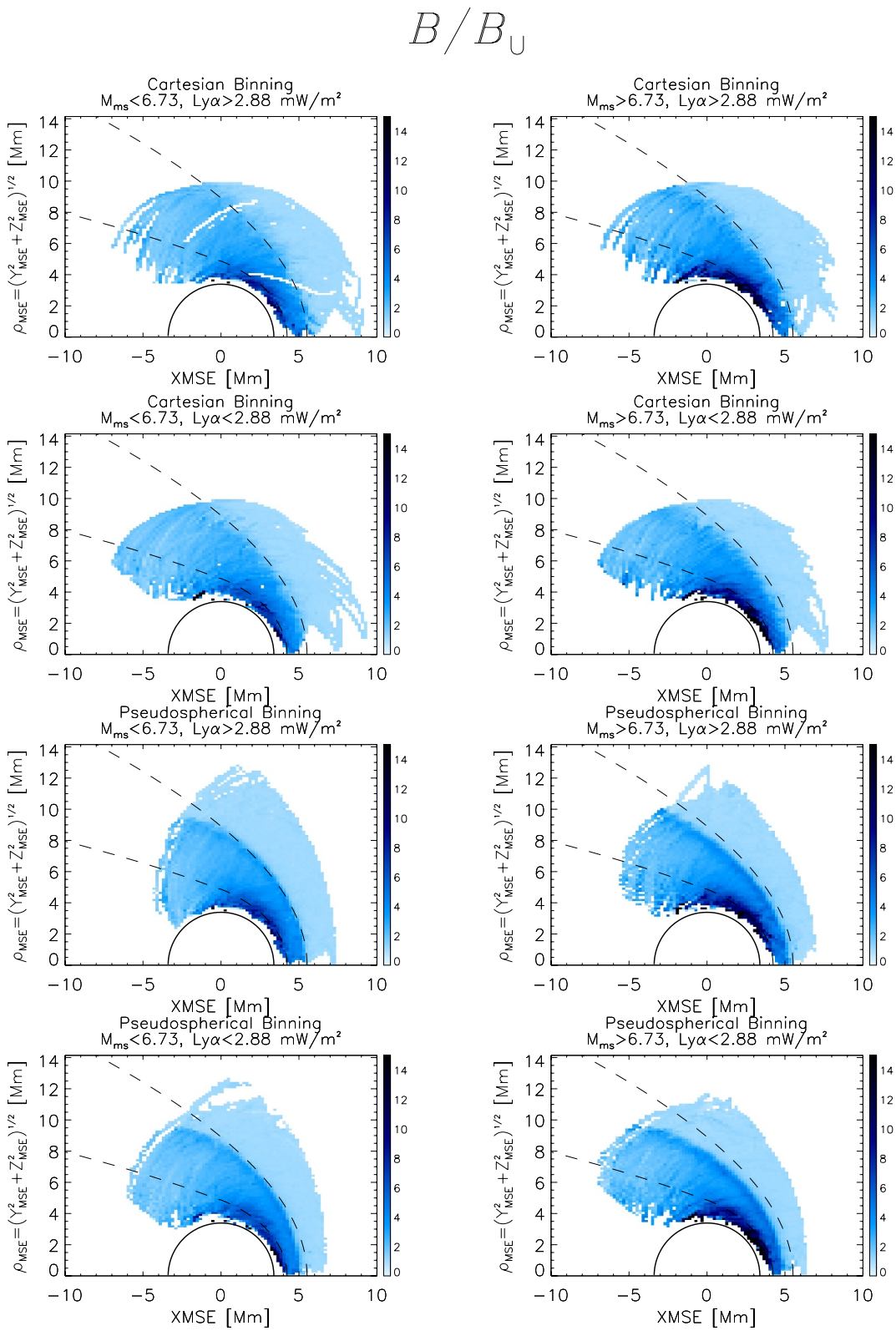

Figure 2. Cylindrical coordinate projection of the global magnetic compression B/B_U as measured by 4270 MAVEN half orbits in cadres of high and low M_{ms} and Lyman Alpha irradiance Lyα. Top four panels show the results of the standard Cartesian binning schema, while the bottom four panels show the results of our implementation. The dotted lines show for comparison the average BS and MPB conics as calculated in Trotignon et al. (2006).

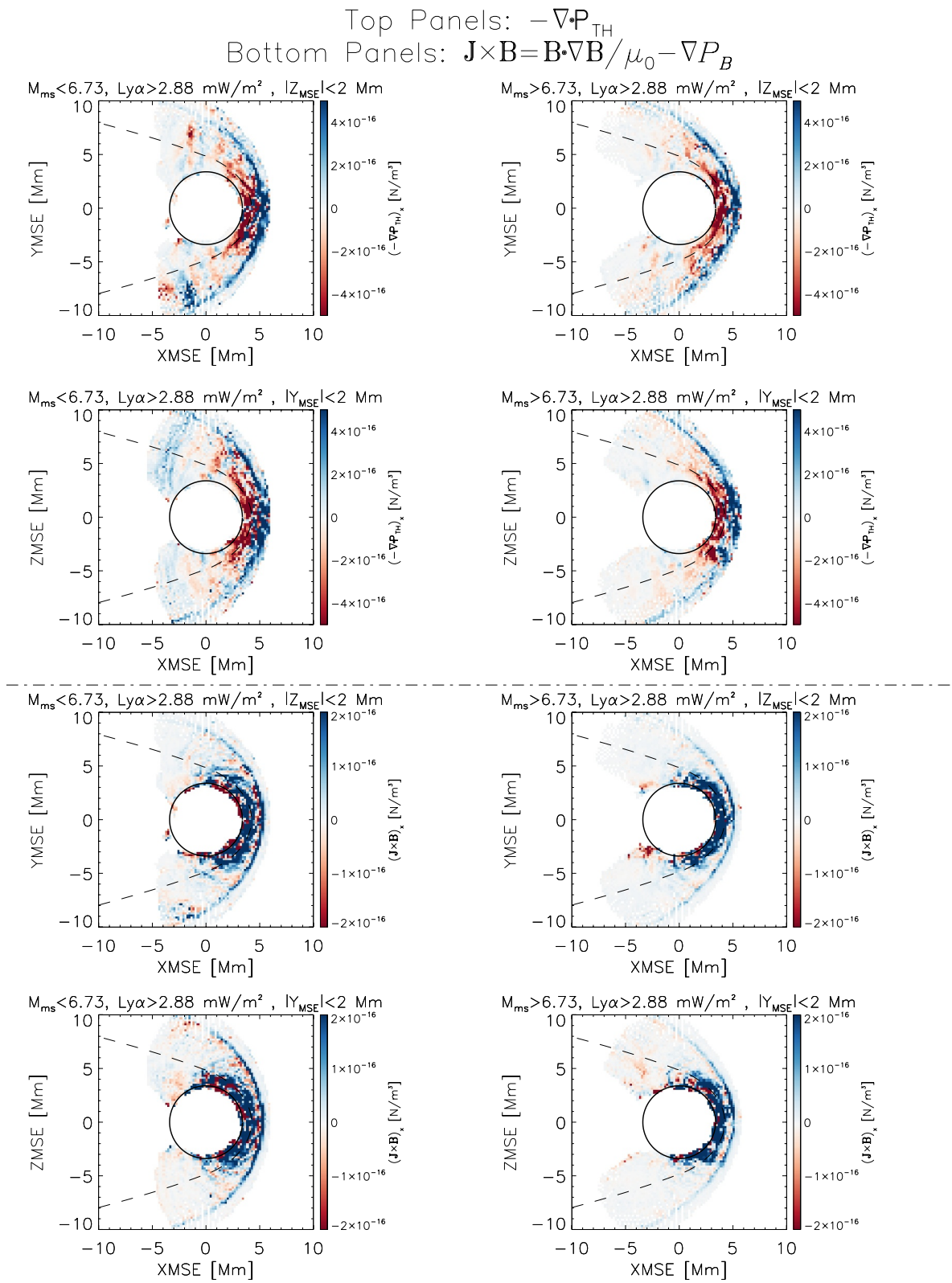

Figure 3. Cross section of forces in the XY and XZ planes for high Lyα cadres, showing only the X component for figure clarity. Top four panels: - Divergence of ion pressure tensor. Bottom four panels: **J** × **B** Force. Forces are calculated within pseudo-spherical position space before being re-binned back to Cartesian space.

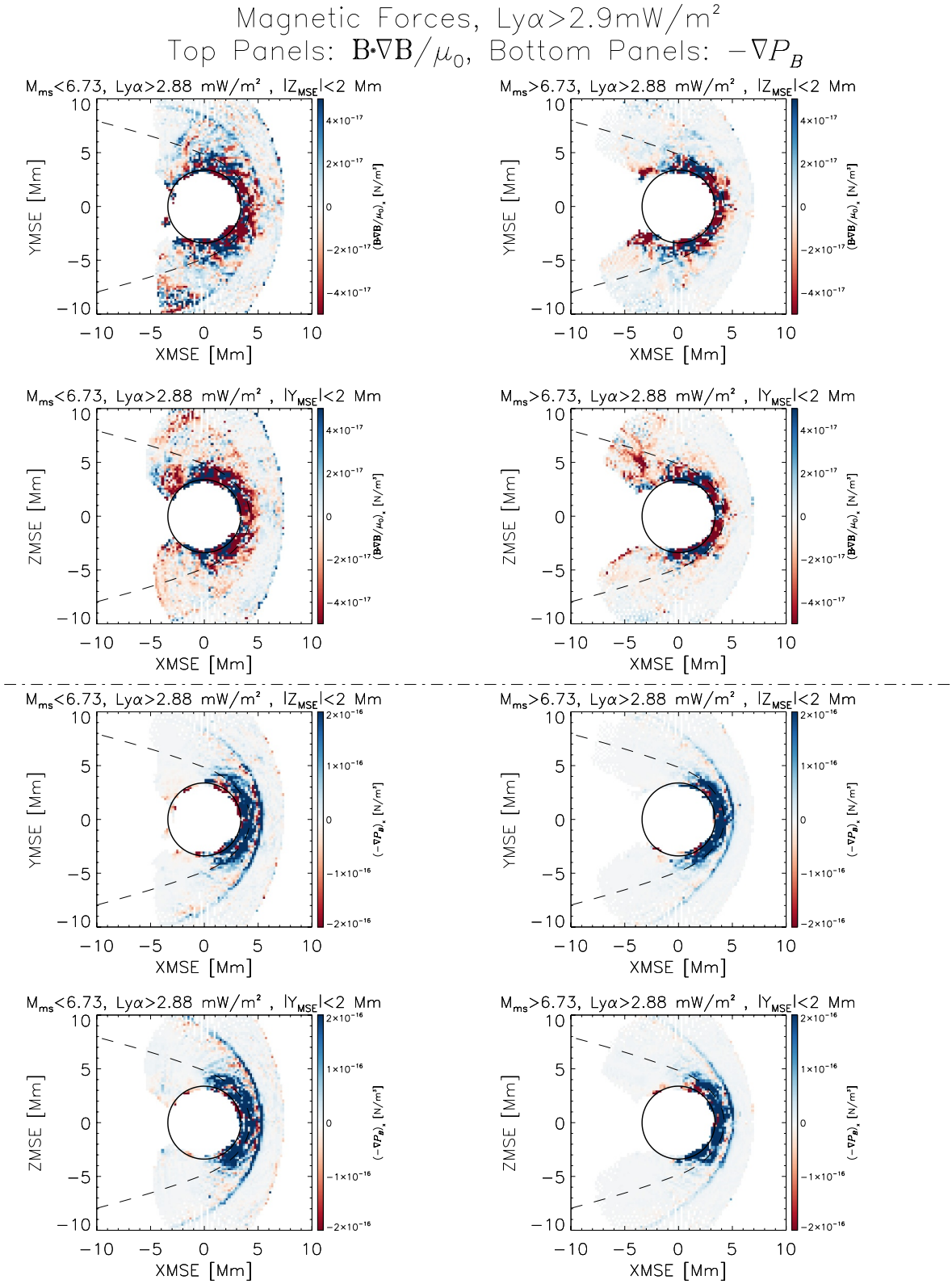

Figure 4. Cross section of the x-components of the $\mathbf{J} \times \mathbf{B}$ force terms for the high Lyα cadres in XY and XZ planes. Top: the magnetic tension $\mathbf{B} \cdot \nabla \mathbf{B}/\mu_0$. Bottom: negative magnetic pressure gradient $-\nabla P_B$.

5.2. Magnetic Pressure Gradient Scaling

The spatial variation of $-\nabla P_B$ is shown in Figure 4 (bottom). We see that the x-component spikes at both the BS and MPB, where the change in B^2 is greatest. As introduced above, this spike at the shock varies with M_{ms}, and can be explained in terms of upstream M_A. Algebraic manipulation gives us

$$\begin{aligned} |-\nabla P_B||_{Dfrac\to 0} &= \left|-\frac{1}{2\mu_0}\nabla\left(B^2\right)\right|\Big|_{Dfrac\to 0} \\ &= \left|-\frac{1}{2\mu_0}\nabla\left(\langle B\rangle_U^2\left(\frac{B}{\langle B\rangle_U}\right)^2\right)\right|\Big|_{Dfrac\to 0} \\ &= \left|-\nabla\left(P_{B_U}\left(\frac{B}{\langle B\rangle_U}\right)^2\right)\right|\Big|_{Dfrac\to 0} \end{aligned} \tag{11}$$

By comparing with parameters in the dataset Fruchtman (2023), we can show that both $\langle B\rangle_U$ and $\left(\frac{B}{\langle B\rangle_U}\right)\Big|_{Dfrac\to 0}$ hold a power relationship with M_A. Here we define $M_A = |\langle \mathbf{V}^{ion}\rangle_U \cdot \hat{\mathbf{n}}_{BS}|/V_A$ as calculated for Fruchtman et al. (2023). There, the shock normal vector $\hat{\mathbf{n}}_{BS}$ was determined by taking the normalized component wise average of the three single spacecraft mixed-mode formulae given in Schwartz (1998). First, we note from the dataset that $\langle B\rangle_U$ increases linearly with $\sqrt{\langle n^{ion}\rangle_U}|\langle \mathbf{V}^{ion}\rangle_U|$ (Pearson correlation $r = -0.593$). This means that - ignoring the $\cos(\theta_{VN})$ term - $P_{B_U} \coloneqq \langle B\rangle_U^2/(2\mu_0)$ can generally be said to power scale with M_A alone. Fitting the power-law relationship $\log M_A$ versus $\log P_{B_U}$ to a linear trend line, we find that $P_{B_U} \approx 8.43 \times 10^{-11} M_A^{-1.45}$Pa. Second, we note that the ramp for a supercritical quasiperpendicular shock is a kinetic scale structure (Balikhin & Gedalin, 2022). At this scale, the relevant nearby downstream feature is not the MHD scale downstream region, but the kinetic scale overshoot structure. We can approximate the magnetic compression in the middle of the ramp to lowest order as halfway between uncompressed $(B/B_U = 1)$ and maximally compressed $(B/B_U = B_{\max}/B_U)$: $B(D_{frac} \to 0)/B_U = (B_{\max}/B_U + 1)/2$. Comparing derived quantities from the above dataset (for $B_{\max}$ determined from 1 s resolution time-series data) as well as Quest (1986); Mellott and Livesey (1987), we see a significant correlation between M_A and $B_{\max}/\langle B\rangle_U$ ($r = 0.817$). Fitting the power law relationship, we find that $B_{\max}/\langle B\rangle_U \approx 0.796 M_A^{0.896}$.

Finally, we must account for the inverse length scale at the shock ramp $\nabla \sim L^{-1}$. Burne et al. (2021); Hobara et al. (2010) showed that the ramp thickness can be at scales between the ion inertial length (c/ω_{pi}) and the electron inertial length (c/ω_{pe}). Hobara et al. (2010) further demonstrated that, in units of inertial length, the ramp scale drops with increasing M_A. However, this comes from a 1D analytical theory which does not take all the physics into account. It has been clearly shown at Earth from multi-spacecraft data by Mazelle and Lembège (2021) that even hybrid code simulations cannot resolve the physical scale of the ramp. They found that the above approximate power law relationship of $L/(c/\omega_{pi})$ versus M_A is really only an upper bound and that the ramp width varies with time and upstream parameters with a maximum close to a few electron inertial lengths. In a study analyzing the length of the quasiperpendicular shock foot, Balikhin and Gedalin (2022) chose a setup in which the length of the ramp resolved to approximately one tenth of the ion Larmor radius r_{Li}, which is in relative agreement with the above Mazelle and Lembège (2021) scale. This quantity is relatively simple to determine power scaling for: $\nabla \sim L^{-1} \approx 10 r_{Li}^{-1} \propto B_U/|\mathbf{V}_U^{ion} \cdot \hat{\mathbf{n}}_{BS}|$, which clearly scales approximately as M_A^{-1}. Fitting the power law relationship of r_{Li} and M_A, we find that $r_{Li}^{-1} \approx 7.91 \times 10^{-6} M_A^{-0.965}\mathrm{m}^{-1}$.

Putting these together, we obtain an estimated theoretical force law scaling behavior at the shock of

$$\begin{aligned} F_{\nabla P_B}^{theo}(M_A) &\approx \frac{10}{r_{Li}} P_{B_U}\left(\frac{1}{2}\left(\frac{B_{\max}}{\langle B\rangle_U}+1\right)\right)^2 \\ &\sim 10 * 7.91 \times 10^{-6} M_A^{-0.965} 8.43 \times 10^{-11} M_A^{-1.45}\left(\frac{1}{2}\left(0.796 M_A^{0.896}+1\right)\right)^2 \mathrm{N/m^3} \end{aligned} \tag{12}$$

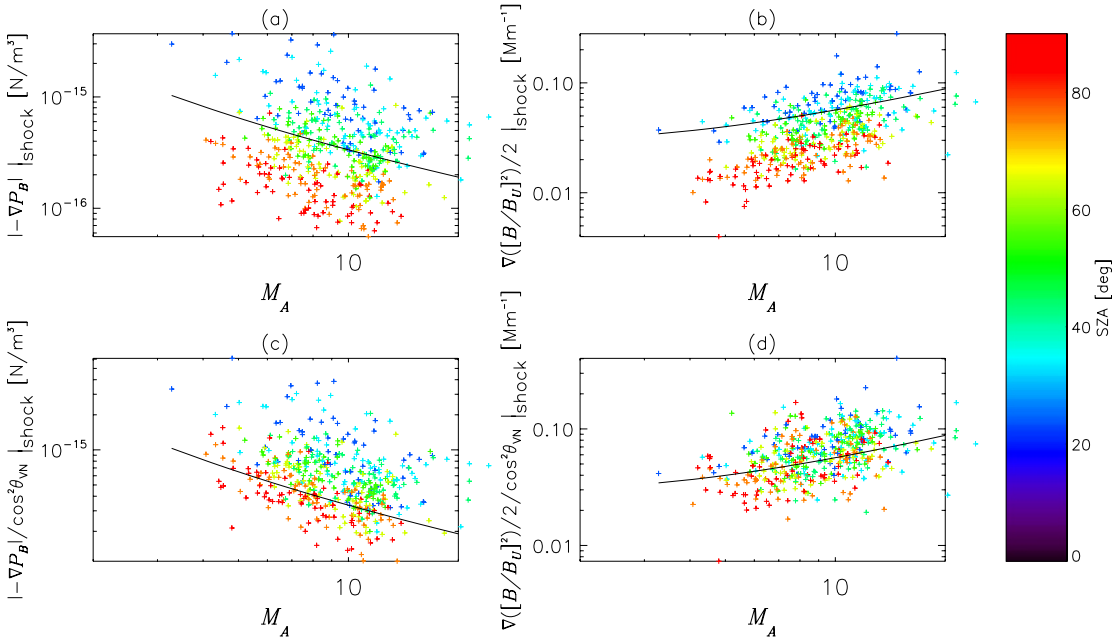

Figure 5. Scaling of magnetic pressure gradient at the shock with M_A, along with theoretical deduction curve. (a) Data points show the measured values of $\left| -\nabla P_B \right|\Big|_{shock}$ at associated M_A, and curve shows the predicted theoretical scaling $F^{theo}_{\nabla P_B}(M_A)$. (b) Data points show measured values of $\left| -\frac{1}{2}\nabla\left(\frac{B}{B_U}\right)^2 \right|\Big|_{shock}$ at associated M_A, with theoretical predicted scaling curve. (c) and (d) show the above figures with data divided by local $\cos^2\theta_{VN}$. Data points are colored by the SZA of that measurement, as indicated by colorbar.

To compare with experimental quantities, we use the 3D pseudo-spherical coordinate space arrays of $|-\nabla P_B|$ and half-orbit characterizing upstream M_A in each cadre. For each column of fixed SZA and ϕ_{MSE} within the range $|D_{frac}| < 0.04$, we find the cell with the maximum $|-\nabla P_B|$ and record the associated value of M_A in the corresponding cell. In case our identification of the middle of the shock ramp is imperfect, this still gives us the $|-\nabla P_B|$ and associated M_A at the shock for all angles. To construct a more representative sample set $(\{M_A\},\{F^{\exp}_{\nabla P_B}\})$, we consider from each cadre only cells for angular coordinates $SZA \in \{25, 35, 45, 55, 65, 75, 85\}$ and $|\phi_{MSE}| \in \{25, 45, 65, 85, 105, 125, 145, 165\}$. We plot them together in Figure 5a. Qualitatively, they are in relatively good agreement, though this has a large data envelope.

B^2 is a dimensional quantity. By the principle of dimensional analysis any dynamical system of dimensional quantities can be simplified into a system involving a smaller number of dimensionless quantities (Barenblatt, 1996; Buckingham, 1914). In the physics of collisionless shocks, two dimensionless quantities related to B^2 are known to jump rapidly in the direction of the shock: First, the magnetic compression B/B_U; second, the ratio of the magnetic pressure to the upstream dynamic pressure P_B/P_{D_U}. Dimensional analysis suggests that it should be the gradient of one of *these*, not B^2 itself that is the source of the sudden outward force. We consider as an example the magnetic compression normalization: Dividing ∇P_B by $2P_{B_U}$ we get a quantity $-\frac{1}{2}\nabla\left(\frac{B}{B_U}\right)^2$ whose theoretical scaling at the shock reduces to dividing Equation 12 by the scaling term $2P_{B_U}$.

The experimental measurements of this normalized force and the theoretical predictions are shown in Figure 5b as the data points and curve, respectively. It is clear that the data envelope is much thinner with this normalization. However, we see that when we normalize our data to consider only compression effects, the slope of the measured distribution is substantially different from that of the theoretical model.

We can account for this anomaly by considering the spatial variation of our measurements and the geometry of the system. In both panels, we color our data points by their SZA. From the color gradient - which is roughly perpendicular to the theoretical curves, we see that the magnetic pressure gradient decreases with SZA. By association (taking Vu mainly along x), this is also a decrease with $\cos^2\theta_{VN} = \left(\mathbf{V}^{ion}_U \cdot \hat{\mathbf{n}}_{BS}/|\mathbf{V}^{ion}_U|\right)^2$ which we

neglected in our power law predictions. At the shock, $-\nabla P_B$ (and $-\nabla \cdot \mathsf{P}_{\mathsf{TH}}$) balances the normal force exerted by the upstream dynamic pressure. Since the latter depends on $\cos^2\theta_{VN}$, then so should the former. Evidence for this can be found in Fruchtman et al. (2023), where the magnetic compression across the shock was found to decrease with SZA for much the same reason. To test this, we normalize the data of panels (a) and (b) by associated values of $\cos^2\theta_{VN}$. The results are shown in panels (c) and (d). We see that the spread in the data has dropped significantly within both the unnormalized and P_{B_U} normalized results. In addition, we see in panel (d) that the latter set of data now closely follows the deduced power law scaling.

5.3. Normalized Total Force

Dimensional analysis can be applied to our statistical analysis and the study of the forces in the magnetosheath more broadly. The Rankine Hugoniot jump conditions tell us that it is not the dimensional downstream MHD variables which are constrained by upstream conditions, but their ratios compared to their upstream counterparts which are constrained (Russell et al., 2016). It is also understood from the energy density perspective that the system scales are governed by boundaries created where pressures balance. At the shock, this is where $P_{D_U} = P_B + P_{TH}$, or dimensionlessly, where $P_B/P_{D_U} + P_{TH}/P_{D_U} = 1$. By principle of dimensional analysis, the dimensionless quantities that vary with respect to dimensionless upstream parameters are $\widetilde{P_B} \coloneqq P_B/P_{D_U} \sim 1/M_A^2$ (or $B/B_U = \sqrt{P_B/P_{B_U}}$) and $\widetilde{\mathsf{P}_{\mathsf{TH}}} \coloneqq \mathsf{P}_{\mathsf{TH}}/P_{D_U} \sim 1/M_S^2$ rather than P_B, and P_{TH}. In the case of the magnetic pressure, we can reasonably extend the argument to hypothesize that the dimensionless quantity $\widetilde{\mathbf{B}} \coloneqq \mathbf{B}/\sqrt{\mu_0 P_{D_U}}$ should also be constrained by upstream quantities.

A ramification of this is that a potential systematic error can arise when numerically calculating downstream forces: When calculating the force in some cell, we must compare the adjacent cells to each other. But these cells may contain data from different orbits with extremely different dimensional upstream parameters (e.g., the same quantity as measured upstream, and/or upstream dynamic pressure). Since the ratios of dimensional downstream parameter to same dimensional upstream parameter are constrained by dimensionless upstream conditions, this can result in significantly different adjacent cells (or even extended gradients over a range of cells) even if no such structure existed within the local plasma measured by either cell. The vertical stripes of alternating positive and negative $(\nabla \cdot \mathsf{P}_{\mathsf{TH}})_X$ seen in Figure 3 are examples of this. While normalizing the equations of our forces by a spatially constant variable to make the system dimensionless will not change the dynamics of the system, proper choice of constant will allow us to constrain our measurements for more accurate force calculation. In addition, if the normalization parameter is chosen properly for the system to constrain the measured dimensional quantity, then the observed trends should hold for *all* (reasonable) values of this parameter. To analyze the total force experienced by ions in the plasma, the reasonable choice of normalization condition to constrain both $\nabla \cdot \mathsf{P}_{\mathsf{TH}}$ and $\mathbf{J} \times \mathbf{B}$ is the upstream dynamic pressure P_{D_U}. Because we are already using scale-normalized dimensionless position variables, our scale normalization framework should itself serve as a proxy to normalizing away the remaining inverse length scale associated with ∇. Note that as binning and force calculation are noncommutative operations, we define

$$\widetilde{\mathbf{J} \times \mathbf{B}} \coloneqq \widetilde{\mathbf{B}} \cdot \nabla \widetilde{\mathbf{B}} - \nabla \widetilde{P_B} \tag{13}$$

As such, rather than considering the spatial variation in $\mathbf{F}_{tot} = \mathbf{J} \times \mathbf{B} - \nabla \cdot \mathsf{P}_{\mathsf{TH}}$, we will instead analyze the dynamics of the total normalized force $\widetilde{\mathbf{F}}_{tot} \equiv \mathbf{F}_{tot}\text{“}/P'_{D_U} = \widetilde{\mathbf{J} \times \mathbf{B}} - \nabla \cdot \widetilde{\mathsf{P}_{\mathsf{TH}}}$. This should work to increase the overall clarity in spatial trends. We demonstrate the improvement in clarity between $\nabla \cdot \mathsf{P}_{\mathsf{TH}}$ and $\nabla \cdot \widetilde{\mathsf{P}_{\mathsf{TH}}}$ in the supporting document. Note that this difference is calculated while still in pseudo-spherical coordinates and before re-binning. The spatial variation in the total normalized force is shown in Figure 6. Once again, we show only the high Lyα cadres.

As stated above, shock forces act to balance out the normal force produced by the upstream dynamic pressure. This means that these forces too should be normal to the BS surface. At MHD scale, it is these forces which accelerate the (fluid scale) SW to rapidly slow its -X directed velocity. These normally directed forces (and thus acceleration) clearly can also have large non-X components. Our spatial mapping of normalized forces makes it easier to visualize that the shock itself diverts the plasma to deflect it around the planet. This is in good agreement with gas-dynamic models of the Earth BS total force (Y. Wang et al., 2004). In the sheath, we see that all components of $\widetilde{\mathbf{F}_{tot}}$

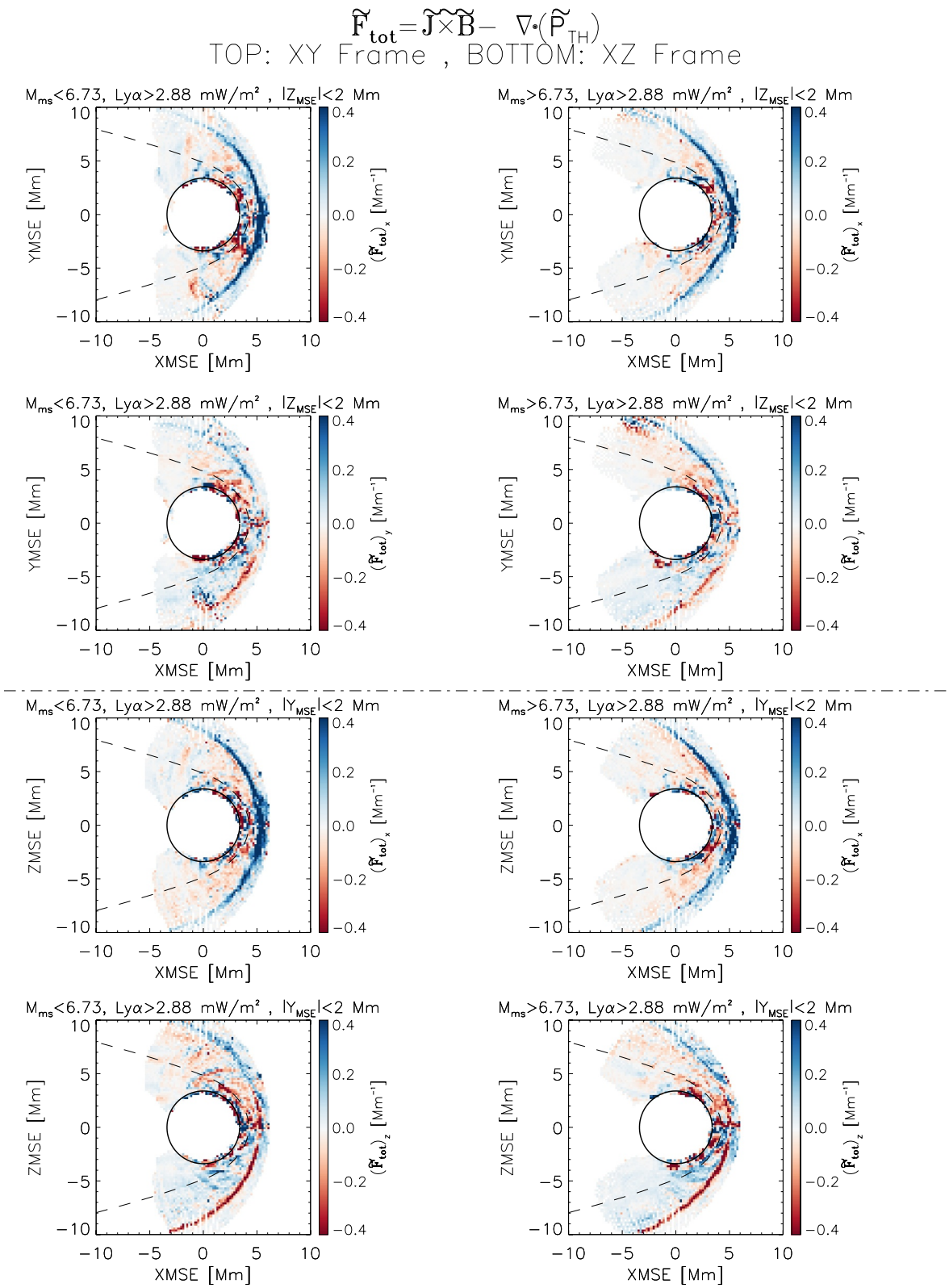

Figure 6. XY and XZ plane cross-sections of the normalized total force $\widetilde{\mathbf{F}}_{tot}$ experienced by ions in the plasma for high EUV cadres. Top and bottom panels show the X and Y/Z components of the force respectively.

are much weaker than at the shock. As seen from the positive $\left(\tilde{F}_{tot}\right)_Y \left(\left(\tilde{F}_{tot}\right)_Z\right)$ values for YMSE (ZMSE) < 0, and negative values for YMSE (ZMSE) > 0, the total force in the magnetosheath flanks acts to keep the plasma contained within the region. We can now see more clearly that it is the BS, rather than the magnetosheath, which contributes most strongly to deflecting the solar wind around Mars. The high resolution view of low SZA magnetosheath forces seen in Y. Wang et al. (2004) shows that Earth $\mathbf{F}_{tot}$ points away from the sun-planet line. Note that the planar cross sections in our off-axis figures are clearly of poor resolution at low SZA.

We further note the presence of an off-axis component azimuthal asymmetry in the forces at the BS. While extant in all hemispheres, this is most visible below the *x*-axis of the XZ and XY planes where the -Z directed component of the force in the -Z surface of the BS is significantly stronger than the -Y directed component in the -Y surface of the BS. This asymmetry is visibly larger than the variation with M_{ms}. This is a result of an azimuthal asymmetry in $\nabla \cdot \widetilde{\mathsf{P}_{\mathsf{TH}}}$, which is more significantly pronounced than an associated asymmetry in $\mathbf{J} \widetilde{\times} \mathbf{B}$ (both not shown). There are two sources of this, experimental and physical respectively. Experimentally, there are immediate difference in data coverage at the shock. In the XZ plane, there is much more coverage, whereas the coverage in XY is spotty near the shock, likely due to a combination of the MAVEN orbit and the prevailing IMF direction. When calculating forces, missing data is filled in by smoothing which tends toward more gradual and less sharp transitions - which occur more often in XY than XZ. Thus XZ has more sharp discontinuities and XY more gradual transitions.

Also considerable is the physical source of this asymmetry: Comparing our unnormalized forces, we saw that $\nabla \cdot \mathsf{P}_{\mathsf{TH}}$ dominates over $\mathbf{J} \times \mathbf{B}$ at the shock. This should remain true after normalizing by the same upstream parameter P_{D_U} to obtain $\nabla \cdot \widetilde{\mathsf{P}_{\mathsf{TH}}}$ and $\mathbf{J} \widetilde{\times} \mathbf{B}$. This normalization choice involves dividing by $m_p \langle n_{SW} \rangle_U$, and so we can rule out a density dependency as the source of this asymmetry. Thus, the asymmetry in the divergence of P_{TH} must be dominated by (tensorial) temperature variations. In general, the off-diagonal components of the pressure tensor are negligible compared to the diagonal components. Thus we can say that $\nabla_i P^{ij}$(with index summation) $\sim$ $\nabla_j P^{jj}$(without index summation). Comparing the off-axis diagonal components $\left(\widetilde{\mathsf{P}_{\mathsf{TH}}}\right)^{yy}$ and $\left(\widetilde{\mathsf{P}_{\mathsf{TH}}}\right)^{zz}$ in the XY and XZ planes respectively, we found that $\left(\widetilde{\mathsf{P}_{\mathsf{TH}}}\right)^{yy} < \left(\widetilde{\mathsf{P}_{\mathsf{TH}}}\right)^{zz}$ at the shock. This should not be surprising: ZMSE is defined as perpendicular to $\vec{B}_{IMF}$, while YMSE is in the plane of $\vec{B}_{IMF}$. Notably, the IMF cone angle at Mars is typically around 60° or 120°, meaning that $\hat{B}_{IMF}$ is 60° off from the XMSE axis, and so - by geometry - must be only around 30° off of the YMSE axis. Thus $\widetilde{\mathsf{P}_{\mathsf{TH}}}^{zz}$ corresponds to the perpendicular component of the anisotropic pressure tensor while $\widetilde{\mathsf{P}_{\mathsf{TH}}}^{yy}$ is a mix of perpendicular and parallel components - primarily the latter. Thus, we find that in the MSE frame $\left(\widetilde{\mathbf{F}_{t\alpha}}\right)_z > \left(\widetilde{\mathbf{F}_{t\alpha}}\right)_y$ due to the temperature anisotropy $T_\perp > T_\parallel$.

Because we have normalized the thermal pressure by the proper upstream normalization parameter which sets the downstream behavior of the system, dimensional analysis tells us that the asymmetry observed here should be always be present.

Romanelli et al. (2020) analyzed the spatial variation of plasma data with different ion species considered separately rather than using this paper's single ion approximation. Doing so, they showed that the velocity in the martian magnetosheath is azimuthally asymmetric due to a mass loading force. The asymmetry in the ion pressure divergence discussed above should contribute to additional velocity asymmetries in individual ion species velocity flows.

5.4. Thermalization and Plasma Instability

It is well established that the size of the Martian magnetosheath is on the order of the convected ion gyroradius (Brecht, 1990; Moses et al., 1988), and thus the downstream plasma barely has time to thermalize. Our scale normalization technique allows us to analyze the thermalization process with considerable precision. Given time for wave-particle interactions, the plasma should then slowly isotropize as it flows away from the shock. We show confirmation of this in Figure 7(top). Here, we define $T_{i\perp}$ as in Halekas, Brain, et al. (2017).

As expected, we see a sharp spike in the anisotropy at the shock, followed by gradual decrease. In all cases, A_i is significantly larger at low SZA, given the shock is stronger there (Fruchtman et al., 2023). Comparing cadres, we also see that A_i appears to drop more rapidly for high M_{ms}.

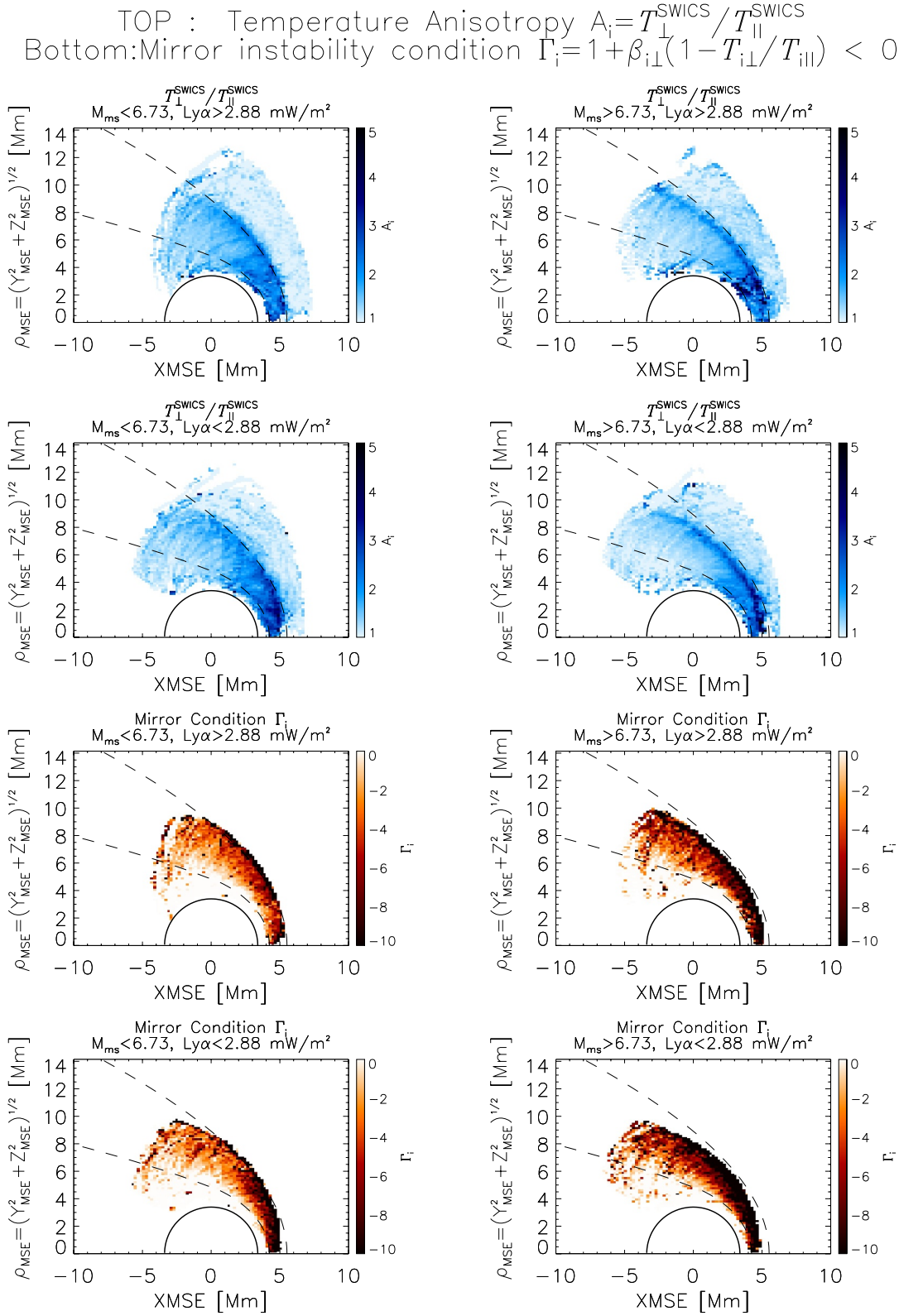

Figure 7. Top panels: The spatial distribution of the ion temperature anisotropy as calculated from the SWICS dataset for our selected half orbits in each cadre. Bottom panels: The spatial distribution of the mirror instability condition $\Gamma_i < 0$ for our selected half orbits in each cadre. Note that, being calculated from instantaneous SWICS mode data - which is primarily intended for sub-BS measurement, the upstream measurements are not fully precise.

The different rates at which the anisotropy collapses can be explained in terms of the mirror instability condition $\Gamma_i = 1 + \beta_\perp(1 - A_i) < 0$ (Hellinger, 2007). Here, $\beta_\perp = 2\mu_0 n_{ion} T_{i\perp}/B^2$, using the above definition of $T_{i\perp}$. When Γ_i is negative, the mirror mode grows and the plasma isotropizes until mirror stability occurs at $\Gamma_i \geq 0$(Hellinger, 2007; Jin et al., 2022). Note that this classical theoretical mirror instability criterion is only valid when ion distributions can be well-described by bi-Maxwellians. There is a more general criterion taking into account the real velocity distribution function (vdf). Though the ions do not all have Maxwellian vdfs (especially for larger amount of pickup ions, including protons, for larger exospheric hydrogen densities near perihelion and at large Lyα), the major part of the ion populations here can be approximated by bi-Maxwellians.

The spatial variation of Γ_i is shown in Figure 7 (bottom). We see that Γ_i approaches zero toward the MPB and higher SZA. Comparing cadres, this trend toward zero can be seen to slow with increasing M_{ms}. Downstream β increases with upstream M_{ms} (Gary et al., 1993; Halekas, Brain, et al., 2017). At high beta a smaller anisotropy is unstable. Thus, starting with the same anisotropy at the shock, it is going to be harder to reach mirror stability at higher beta.

That A_i and Γ_i gradually change over a large spatial range is a good reminder that instabilities do not process the plasma instantaneously. Plasma modifications generated by instabilities have finite growth rates which implies finite growth lengths. For an anisotropic plasma, the mirror mode instability has the largest growth rate, which obeys (Hellinger, 2007; Jin et al., 2022):

$$\gamma_{\max} = \frac{\omega_{ci}}{4\sqrt{3\pi}} \frac{\Gamma_i^2}{\beta_{i\perp}\sqrt{A_i^3\left(1 + \beta_{i\perp}\left(1 - A_i^{-1}\right)/2\right)}} \tag{14}$$

This growth should occur until mirror stability is achieved or the mirror mode has saturated the plasma. The spatial distribution of $\gamma_{\max}$ is shown in Figure 8 (top). Note that the time-series $\gamma_{max}(t)$ has been set to zero when $\Gamma_i(t) \geq 0$. Because γ_{max} spatially varies by orders of magnitude, calculating the mean of pseudo-spherical bins when re-binning to Cartesian bins can introduce a large upward bias. To avoid this, we instead re-bin by filling Cartesian cells with the *median* value of the associated pseudo-spherical cells. We see that γ_{max} drops by orders of magnitude with distance from the BS, and rapidly decreases as plasma progresses through the sheath. This is in agreement with Jin et al. (2022); Simon Wedlund et al. (2022) where mirror mode structures were seen in the upper magnetosheath. Comparing upstream conditions, we see that γ_{max} is larger in high M_{ms} cadres at the BS.

As plasma instability modes grow exponentially, we can approximately quantify the thermalization process in terms of the number of instability growth periods experienced as the plasma travels through the sheath. At a single growth period, the instability mode has made one e-fold, and by this point we can say that the plasma has sufficient time to begin thermalizing. Similarly, as the number of e-folds becomes large, the unstable mode should approach saturation.

$\gamma_{\max}$ is not constant throughout the plasma, and thus we cannot simply compare the growth rate to the time in which the plasma flows through the sheath. Instead we must integrate γ_{max} over time, following along flow lines. This will give us the number of e-folds as we progress through the plasma. To follow along flow lines, we start by rebinning our spatial distribution of the ion velocity and γ_{max} into 3D Cartesian components to obtain $\mathbf{V}(\mathbf{x})$ and $\gamma_{max}(\mathbf{x})$. In order to fill the spatial distribution, we NAN-fill these resulting Cartesian arrays using analogous methods to those described above. For each integer degree of SZA, we start at the shock surface, $\phi_{MSE} = -135°$, and increment in $\delta t = 50ms$ timesteps using the fourth-order Runge-Kutta method (Joy, 2007). Here, we have arbitrarily chosen $\phi_{MSE} = -135°$ as a starting azimuth between the Y and Z axis. We use $\delta t = 50ms$ as a timestep sufficiently well below the relevant timescales as to allow fine scale integration of e-folding and minimize cells skipped by Runge-Kutta flowlines. At each time step $t = \iota\delta t$, we then increment the number of e-folds since leaving the shock by $\gamma_{max}(\mathbf{x})\delta t$. This is plotted in Figure 8 (bottom). Here, each cell shows the number of e-folds generated between the start of the flow line up until the time step in which the flow line leaves that cylindrical coordinate cell. For each cadre, the dotted lines show the cylindrical projections of the longest flow lines for intervals $SZA < 16°$, $16° \leq SZA < 40°$, $40° \leq SZA < 66°$, $66° \leq SZA < 90°$ and $90° \leq SZA < 116°$. We briefly note that the differences in the e-folding gradients between cadres are more due to inhomogenious noise than any upstream phenomena; all cadres are shown here for completeness.

Comparing the e-folding gradients along different flow line trajectories, we see that the e-folding rate varies with starting SZA: thermalization begins closer to the shock near the nose than toward the flanks. At sufficiently high

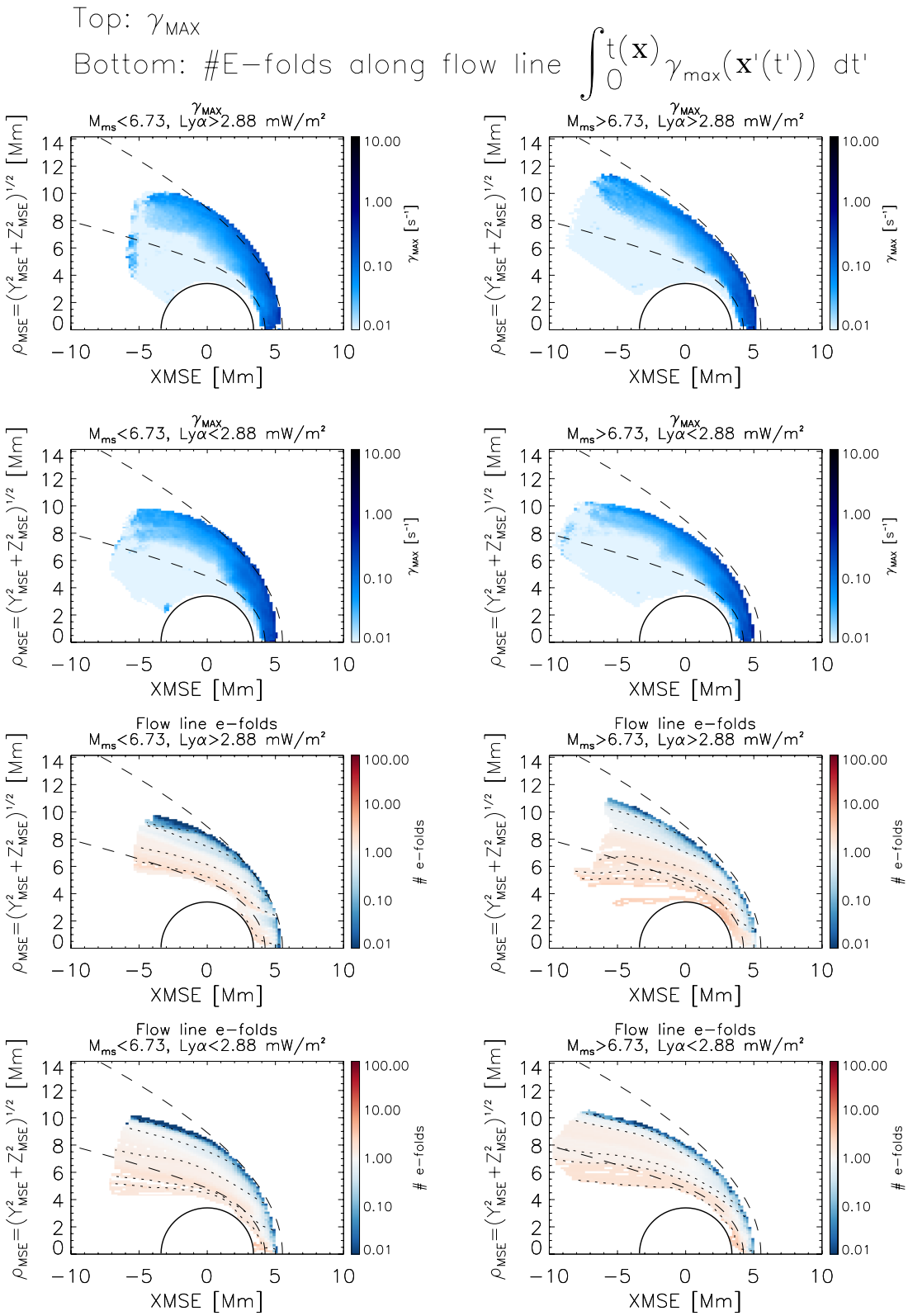

Figure 8. Top panels: The spatial distribution of the maximum growth rate γ_{max} in the plasma. Bottom panels: The number of e-folds in the mirror mode generated since leaving the shock surface until reaching that point in space along a calculated flow line. The dotted lines show example flow lines.

SZA, the plasma never appears to reach the e-folding regime at all. Note that this is not merely a result of flow lines at the flanks starting further along: there is a clear one e-fold band (in white) that follows a flow path-like trajectory.

That the e-folding happens more quickly at the nose than near the flank can be explained in terms of the velocity gradient. As seen above, plasma is significantly slowed down at the shock. As more deflection is necessary near the nose than at the flanks to avoid the ionosphere, $\mathbf{V}$ drops more significantly. $\mathbf{V}$ is (relatively) small close to the shock. As the plasma is re-accelerated and travels through the sheath, γ_{max} drops by orders of magnitude with distance from the BS. Depending on the starting SZA, our flowlines can travel for $\sim 30 - 80$ seconds through the binned magnetosheath before running out of data (a figure for which is shown in the Supporting document). By comparison, we found that ~ 1 second is spent near the outer boundary where γ_{max} is at a local maximum. While this may seem insignificant, a majority of the γ_{max} weighted average of the duration is spent in this region. $\mathbf{V}$ is smaller near the nose for longer and farther compared to at the flanks, where the plasma is closer to the outer boundary and γ_{max} is larger. At the flanks, $\mathbf{V}$ is sufficiently large that the plasma quickly enters a region with small γ_{max} long before e-folding can properly begin. With this analysis, we see that there is a region of persistent anisotropy that never gets wiped out by instabilities.

A related statistical analysis of the spatial distribution (using Cartesian coordinate binning) of Martian mirror mode structures was conducted by Simon Wedlund et al. (2023). They found two main regions of high occurrence of mirror mode waves: one just downstream of the nominal BS which corresponds to where the instability condition is more negative and where the Mirror Mode structures should be more likely created and a second one just around the MPB where an accumulation of evolved structures is expected as for the terrestrial magnetopause. The former is in good agreement with our results herein, though we see no evidence of the latter.

6. Conclusion

As has been demonstrated, the length scale normalization binning technique allows for higher resolution analysis of magnetosheath plasma compared to the traditional Cartesian binning schema. Our implementation of this technique as applied to the Martian system makes clear a number of features that were previously imperceptible: we can resolve spatial structures that were previously washed out. The magnetic tension $\mathbf{B} \cdot \nabla \mathbf{B}/\mu_0$ has been found to be insignificant at the shock, and only become prominent deeper into the magnetosheath. The unnormalized magnetic pressure gradient $-\nabla P_B$ was shown to be the $\mathbf{J} \times \mathbf{B}$ term which is prominent at the shock and decreases in magnitude with M_{ms} and M_A. By utilizing dimensional analysis to constrain B, we found that the gradient in magnetic compression can be described almost entirely in terms of a M_A power law relationship. The ion thermal pressure divergence $-\nabla \cdot \mathsf{P}_{\mathsf{TH}}$ can now be observed to possess an azimuthal asymmetry at the shock. Proper use of dimensional analysis shows that this arises from the plasma temperature anisotropy. Finally, we found that thermalization of the Martian magnetosheath is heavily dependent on upstream Mms and the SZA of the incoming flow. This is explained mainly in terms of the ion velocity distribution.

It should be noted that the implementation of our technique is highly simplified. Given more precise parametrization of BS taking into account larger number of upstream parameters and crustal fields, and an associated highly parameterized MPB surface, future investigations (either as a follow up or as a counterpart study for other systems with induced magnetosheaths) could rework our framework to properly set a coordinate following the fractional distance between magnetosheath boundaries for even higher resolution. As an alternative to the scale normalized fractional distance implemented here, another possible implementation is to use $D_{frac} = (\mathbf{X} \cdot \hat{\mathbf{n}} - R_{BS})/r_{Li_U}$, the distance from the shock in upstream Larmor radii in the shock normal direction. Structures such as the overshoot have a thickness which are on the order of the convective ion Larmor radius, and the outer boundary sets initial conditions, thus the rigorously defined distance from the outer boundary may potentially precisely capture kinetic scale magnetosheath processes. Unlike Mars, Venus has a purely extrinsic magnetosheath. This means that the inner and outer magnetosheath boundaries should be more simply parameterized. Thus we expect a Venusian counterpart study using our scale normalization technique would produce more accurate results than our own.

Data Availability Statement

MAVEN data is publicly available through the Planetary Data System (https://lasp.colorado.edu/maven/sdc/public/). We use the SWIA (Halekas et al., 2015) (https://doi.org/10.17189/1414231), SWEA (Mitchell et al., 2016) (https://doi.org/10.17189/1414252), MAG (Connerney et al., 2015) (https://doi.org/10.17189/1517674), and EUVM (Eparvier et al., 2015) (https://doi.org/10.17189/1517693) datasets.

Acknowledgments
We acknowledge NASA and the MAVEN mission for support through grant NNH10CC04C to the University of Colorado and by subcontract to Space Sciences Laboratory, University of California, Berkeley. Parts of this work for the observations obtained with the SWEA instrument are supported by the French space agency CNES (National Centre for Space Studies).

References

Acuña, M., Connerney, J., Wasilewski, P. a., Lin, R., Anderson, K., Carlson, C., et al. (1998). Magnetic field and plasma observations at mars: Initial results of the mars global surveyor mission. *Science*, *279*(5357), 1676–1680. https://doi.org/10.1126/science.279.5357.1676

Azari, A., Abrahams, E., Sapienza, F., Mitchell, D., Biersteker, J., Xu, S., et al. (2023). Magnetic field draping in induced magnetospheres: Evidence from the maven mission to mars. *Journal of Geophysical Research: Space Physics*, *128*(11), e2023JA031546. https://doi.org/10.1029/2023ja031546

Balikhin, M., & Gedalin, M. (2022). Collisionless shocks in the heliosphere: Foot width revisited. *The Astrophysical Journal*, *925*(1), 90. https://doi.org/10.3847/1538-4357/ac3bb3

Barenblatt, G. I. (1996). *Scaling, self-similarity, and intermediate asymptotics*. Cambridge University Press.

Bertucci, C., Mazelle, C., Acuna, M., Russell, C., & Slavin, J. (2005). Structure of the magnetic pileup boundary at mars and venus. *Journal of Geophysical Research*, *110*(A1). https://doi.org/10.1029/2004ja010592

Brecht, S. H. (1990). Magnetic asymmetries of unmagnetized planets. *Geophysical Research Letters*, *17*(9), 1243–1246. https://doi.org/10.1029/gl017i009p01243

Buckingham, E. (1914). On physically similar systems; illustrations of the use of dimensional equations. *Physics Reviews*, *4*, 345–376. https://doi.org/10.1103/PhysRev.4.345

Burne, S., Bertucci, C., Mazelle, C., Morales, L. F., Meziane, K., Halekas, J., et al. (2021). The structure of the martian quasi-perpendicular supercritical shock as seen by MAVEN. *Journal of Geophysical Research (Space Physics)*, *126*(9), e28938. https://doi.org/10.1029/2020JA028938

Connerney, J., Espley, J., Lawton, P., Murphy, S., Odom, J., Oliversen, R., & Sheppard, D. (2015). The maven magnetic field investigation. *Space Science Reviews*, *195*(1), 257–291. https://doi.org/10.1007/s11214-015-0169-4

Crider, D. H. (2004). The influence of crustal magnetism on the solar wind interaction with mars: Recent observations. *Advances in Space Research*, *33*(2), 152–160. Retrieved from (Planetary Atmospheres, Ionospheres and Plasma Interactions) https://doi.org/10.1016/j.asr.2003.04.013

Edberg, N., Lester, M., Cowley, S., & Eriksson, A. (2008). Statistical analysis of the location of the martian magnetic pileup boundary and bow shock and the influence of crustal magnetic fields. *Journal of Geophysical Research*, *113*(A8). https://doi.org/10.1029/2008ja013096

Edberg, N. J. T., Lester, M., Cowley, S. W. H., Brain, D. A., Fränz, M., & Barabash, S. (2010). Magnetosonic mach number effect of the position of the bow shock at mars in comparison to venus. *Journal of Geophysical Research*, *115*(A7). Retrieved from https://doi.org/10.1029/2009JA014998

Eisele, J. A., & Mason, R. M. (1970). *Applied matrix and tensor analysis*. Wiley.

Eparvier, F., Chamberlin, P., Woods, T., & Thiemann, E. (2015). The solar extreme ultraviolet monitor for maven. *Space Science Reviews*, *195*(1–4), 293–301. https://doi.org/10.1007/s11214-015-0195-2

Fang, X., Ma, Y., Masunaga, K., Dong, Y., Brain, D., Halekas, J., et al. (2017). The mars crustal magnetic field control of plasma boundary locations and atmospheric loss: Mhd prediction and comparison with maven. *Journal of Geophysical Research: Space Physics*, *122*(4), 4117–4137. Retrieved from https://doi.org/10.1002/2016JA023509

Fruchtman, J. (2023). Maven shock crossing data [dataset]. *Zenodo*. Retrieved from https://doi.org/10.5281/zenodo.8161688

Fruchtman, J., Halekas, J., Gruesbeck, J., Mitchell, D., & Mazelle, C. (2023). Seasonal and mach number variation of the martian bow shock structure. *Journal of Geophysical Research: Space Physics*, *128*(8), e2023JA031759. https://doi.org/10.1029/2023ja031759

Garnier, P., Jacquey, C., Gendre, X., Génot, V., Mazelle, C., Fang, X., et al. (2022a). The drivers of the martian bow shock location: A statistical analysis of mars atmosphere and volatile evolution and mars express observations. *Journal of Geophysical Research: Space Physics*, *127*(5), e2021JA030147. Retrieved from https://doi.org/10.1029/2021JA030147

Garnier, P., Jacquey, C., Gendre, X., Génot, V., Mazelle, C., Fang, X., et al. (2022b). The influence of crustal magnetic fields on the martian bow shock location: A statistical analysis of maven and mars express observations. *Journal of Geophysical Research: Space Physics*, *127*(5), e2021JA030146. Retrieved from https://doi.org/10.1029/2021JA030146

Gary, S. P., Fuselier, S. A., & Anderson, B. J. (1993). Ion anisotropy instabilities in the magnetosheath. *Journal of Geophysical Research*, *98*(A2), 1481–1488. https://doi.org/10.1029/92ja01844

Gedalin, M. (1996). Ion reflection at the shock front revisited. *Journal of Geophysical Research*, *101*(A3), 4871–4878. https://doi.org/10.1029/95ja03669

Gruesbeck, J. R., Espley, J. R., Connerney, J. E. P., DiBraccio, G. A., Soobiah, Y. I., Brain, D., et al. (2018). The three-dimensional bow shock of mars as observed by maven. *Journal of Geophysical Research: Space Physics*, *123*(6), 4542–4555. Retrieved from https://doi.org/10.1029/2018JA025366

Halekas, J., Brain, D. A., Luhmann, J. G., DiBraccio, G. A., Ruhunusiri, S., Harada, Y., et al. (2017a). Flows, fields, and forces in the mars-solar wind interaction. *Journal of Geophysical Research: Space Physics*, *122*(11), 11320–11341. Retrieved from https://doi.org/10.1002/2017JA024772

Halekas, J., Ruhunusiri, S., Harada, Y., Collinson, G., Mitchell, D., Mazelle, C., et al. (2017b). Structure, dynamics, and seasonal variability of the mars-solar wind interaction: Maven solar wind ion analyzer in-flight performance and science results. *Journal of Geophysical Research: Space Physics*, *122*(1), 547–578. https://doi.org/10.1002/2016ja023167

Halekas, J., Taylor, E., Dalton, G., Johnson, G., Curtis, D., McFadden, J., et al. (2015). The solar wind ion analyzer for maven. *Space Science Reviews*, *195*(1), 125–151. https://doi.org/10.1007/s11214-013-0029-z

Hall, B. E. S., Lester, M., Sánchez-Cano, B., Nichols, J. D., Andrews, D. J., Edberg, N. J. T., et al. (2016). Annual variations in the martian bow shock location as observed by the mars express mission. *Journal of Geophysical Research: Space Physics*, *121*(11), 11474–11494. Retrieved from https://doi.org/10.1002/2016JA023316

Hall, B. E. S., Sánchez-Cano, B., Wild, J. A., Lester, M., & Holmström, M. (2019). The martian bow shock over solar cycle 23–24 as observed by the mars express mission. *Journal of Geophysical Research: Space Physics*, *124*(6), 4761–4772. Retrieved from https://doi.org/10.1029/2018JA026404

Hellinger, P. (2007). Comment on the linear mirror instability near the threshold. *Physics of Plasmas*, *14*(8). https://doi.org/10.1063/1.2768318

Hobara, Y., Balikhin, M., Krasnoselskikh, V., Gedalin, M., & Yamagishi, H. (2010). Statistical study of the quasi-perpendicular shock ramp widths. *Journal of Geophysical Research*, *115*(A11). https://doi.org/10.1029/2010ja015659

Jakosky, B. M., Lin, R. P., Grebowsky, J. M., Luhmann, J. G., Mitchell, D., Beutelschies, G., et al. (2015). The mars atmosphere and volatile evolution (maven) mission. *Space Science Reviews*, *195*(1), 3–48. https://doi.org/10.1007/s11214-015-0139-x

Jin, T., Lei, L., Yiteng, Z., Lianghai, X., & Fuhao, Q. (2022). Statistical analysis of the distribution and evolution of mirror structures in the martian magnetosheath. *The Astrophysical Journal*, *929*(2), 165. https://doi.org/10.3847/1538-4357/ac5f00

Joy, K. I. (2007). *Numerical methods for particle tracing in vector fields* (pp. 1–7). On-Line Visualization Notes.

Kallio, E., Luhmann, J., & Barabash, S. (1997). Charge exchange near mars: The solar wind absorption and energetic neutral atom production. *Journal of Geophysical Research*, *102*(A10), 22183–22197. https://doi.org/10.1029/97ja01662

Kennel, C. F., Edmiston, J. P., & Hada, T. (1985). A quarter century of collisionless shock research. *Washington DC American Geophysical Union Geophysical Monograph Series*, *34*, 1–36. https://doi.org/10.1029/GM034p0001

Kotzé, P. (2023). Hydrogen lyman-alpha periodicity behaviour during various solar cycles. *Astrophysics and Space Science*, *368*(1), 6. https://doi.org/10.1007/s10509-023-04163-9

Luhmann, J., Ledvina, S., & Russell, C. (2004). Induced magnetospheres. *Advances in Space Research*, *33*(11), 1905–1912. Retrieved from (Comparative Magnetospheres) https://doi.org/10.1016/j.asr.2003.03.031

Ma, Y., Nagy, A. F., Sokolov, I. V., & Hansen, K. C. (2004). Three-dimensional, multispecies, high spatial resolution mhd studies of the solar wind interaction with mars. *Journal of Geophysical Research*, *109*(A7). Retrieved from https://doi.org/10.1029/2003JA010367

Marquette, M. L., Lillis, R. J., Halekas, J. S., Luhmann, J. G., Gruesbeck, J., & Espley, J. R. (2018). Autocorrelation study of solar wind plasma and imf properties as measured by the maven spacecraft. *Journal of Geophysical Research: Space Physics*, *123*(4), 2493–2512. https://doi.org/10.1002/2018ja025209

Mazelle, C., & Lembège, B. (2021). Evidence of the nonstationarity of the terrestrial bow shock from multi-spacecraft observations: Methodology, results, and quantitative comparison with particle-in-cell (pic) simulations. *Annales Geophysicae*, *39*(4), 571–598. Retrieved from https://doi.org/10.5194/angeo-39-571-2021

Mazelle, C., Meziane, K., Mitchell, D., Garnier, P., Espley, J., Hamza, A., et al. (2018). Evidence for neutrals-foreshock electrons impact at mars. *Geophysical Research Letters*, *45*(9), 3768–3774. https://doi.org/10.1002/2018gl077298

Mazelle, C., Winterhalter, D., Sauer, K., Trotignon, J., Acuna, M., Baumgärtel, K., et al. (2004). Bow shock and upstream phenomena at mars. *Space Science Reviews*, *111*(1/2), 115–181. https://doi.org/10.1023/b:spac.0000032717.98679.d0

Mellott, M., & Livesey, W. (1987). Shock overshoots revisited. *Journal of Geophysical Research*, *92*(A12), 13661–13665. https://doi.org/10.1029/ja092ia12p13661

Mitchell, D., Mazelle, C., Sauvaud, J.-A., Thocaven, J.-J., Rouzaud, J., Fedorov, A., et al. (2016). The maven solar wind electron analyzer. *Space Science Reviews*, *200*(1), 495–528. https://doi.org/10.1007/s11214-015-0232-1

Moses, S., Coroniti, F., & Scarf, F. (1988). Expectations for the microphysics of the mars-solar wind interaction. *Geophysical Research Letters*, *15*(5), 429–432. https://doi.org/10.1029/gl015i005p00429

Němec, F., Linzmayer, V., Němeček, Z., & Šafránková, J. (2020). Martian bow shock and magnetic pileup boundary models based on an automated region identification. *Journal of Geophysical Research: Space Physics*, *125*(11), e2020JA028509. https://doi.org/10.1029/2020ja028509

Quest, K. B. (1986). Simulations of high mach number perpendicular shocks with resistive electrons. *Journal of Geophysical Research*, *91*(A8), 8805–8815. https://doi.org/10.1029/ja091ia08p08805

Rahmati, A., Larson, D., Cravens, T., Lillis, R., Halekas, J., McFadden, J., et al. (2018). Seasonal variability of neutral escape from mars as derived from maven pickup ion observations. *Journal of Geophysical Research: Planets*, *123*(5), 1192–1202. https://doi.org/10.1029/2018je005560

Ramstad, R., Barabash, S., Futaana, Y., & Holmström, M. (2017). Solar wind- and euv-dependent models for the shapes of the martian plasma boundaries based on mars express measurements. *Journal of Geophysical Research: Space Physics*, *122*(7), 7279–7290. Retrieved from https://doi.org/10.1002/2017JA024098

Romanelli, N., DiBraccio, G., Halekas, J., Dubinin, E., Gruesbeck, J., Espley, J., et al. (2020). Variability of the solar wind flow asymmetry in the martian magnetosheath observed by maven. *Geophysical Research Letters*, *47*(22), e2020GL090793. https://doi.org/10.1029/2020gl090793

Russell, C. T., Luhmann, J. G., & Strangeway, R. J. (2006). The solar wind interaction with venus through the eyes of the pioneer venus orbiter. *Planetary and Space Science*, *54*(13–14), 1482–1495. https://doi.org/10.1016/j.pss.2006.04.025

Russell, C. T., Luhmann, J. G., & Strangeway, R. J. (2016). *Space physics: An introduction*. Cambridge University Press.

Schwartz, S. J. (1991). Magnetic field structures and related phenomena at quasi-parallel shocks. *Advances in Space Research*, *11*(9), 231–240. https://doi.org/10.1016/0273-1177(91)90039-m

Schwartz, S. J. (1998). Shock and discontinuity normals, mach numbers, and related parameters. *ISSI Scientific Reports Series*, *1*, 249–270.

Schwartz, S. J., & Burgess, D. (1991). Quasi-parallel shocks: A patchwork of three-dimensional structures. *Geophysical Research Letters*, *18*(3), 373–376. Retrieved from https://doi.org/10.1029/91GL00138

Simon Wedlund, C., Volwerk, M., Mazelle, C., Halekas, J., Rojas-Castillo, D., Espley, J., & Möstl, C. (2022). Making waves: Mirror mode structures around mars observed by the maven spacecraft. *Journal of Geophysical Research: Space Physics*, *127*(1), e2021JA029811. https://doi.org/10.1029/2021ja029811

Simon Wedlund, C., Volwerk, M., Mazelle, C., Rojas Mata, S., Stenberg Wieser, G., Futaana, Y., et al. (2023). Statistical distribution of mirror-mode-like structures in the magnetosheaths of unmagnetised planets – Part 1: Mars as observed by the maven spacecraft. *Annales Geophysicae*, *41*(1), 225–251. Retrieved from https://doi.org/10.5194/angeo-41-225-2023

Tatrallyay, M., Gevai, G., Apathy, I., Schwingenschuh, K., Zhang, T.-L., Kotova, G., et al. (1997). Magnetic field overshoots in the martian bow shock. *Journal of Geophysical Research*, *102*(A2), 2157–2163.

Trotignon, J., Mazelle, C., Bertucci, C., & Acuña, M. (2006). Martian shock and magnetic pile-up boundary positions and shapes determined from the phobos 2 and mars global surveyor data sets. *Planetary and Space Science*, *54*(4), 357–369. https://doi.org/10.1016/j.pss.2006.01.003

Vignes, D., Acuña, M., Connerney, J., Crider, D., Reme, H., & Mazelle, C. (2002). Factors controlling the location of the bow shock at mars. *Geophysical Research Letters*, *29*(9), 42–51. https://doi.org/10.1029/2001gl014513

Vignes, D., Mazelle, C., Rme, H., Acuña, M. H., Connerney, J. E. P., Lin, R. P., et al. (2000). The solar wind interaction with mars: Locations and shapes of the bow shock and the magnetic pile-up boundary from the observations of the mag/er experiment onboard mars global surveyor. *Geophysical Research Letters*, *27*(1), 49–52. Retrieved from https://doi.org/10.1029/1999GL010703

Wang, M., Xie, L., Lee, L., Xu, X., Kabin, K., Lu, J., et al. (2020). A 3d parametric martian bow shock model with the effects of mach number, dynamic pressure, and the interplanetary magnetic field. *The Astrophysical Journal*, *903*(2), 125. https://doi.org/10.3847/1538-4357/abbc04

Wang, Y., Raeder, J., & Russell, C. (2004). Plasma depletion layer: Magnetosheath flow structure and forces. *Annales Geophysicae*, *22*(3), 1001–1017. https://doi.org/10.5194/angeo-22-1001-2004

Williams, D. R. (2021). *Mars fact sheet - nasa*. NASA. Retrieved from https://nssdc.gsfc.nasa.gov/planetary/factsheet/marsfact.html

Wong, H. (1968). Foot of normal hydromagnetic shock. *Bulletin of the American Physical Society*, *13*, 1518.

Woods, L. (1971). On double-structured, perpendicular, magneto-plasma shock waves. *Plasma Physics*, *13*(4), 289–302. https://doi.org/10.1088/0032-1028/13/4/302

Zhang, T.-L., Schwingenschuh, K., Russell, C. T., & Luhmann, J. G. (1991). Asymmetries in the location of the venus and mars bow shock. *Geophysical Research Letters*, *18*(2), 127–129. Retrieved from https://doi.org/10.1029/90GL02723